The detectability of single- and multiple-planet systems in Gaia data

Martin Gustavsson

Lund Observatory
Lund University

2015-EXA97

Degree project of 15 higher education credits
May 2015

Supervisor: Lennart Lindegren

Lund Observatory
Box 43
SE-221 00 Lund
Sweden

Abstract

The all-sky survey of Gaia will generate vast amounts of astrometric data, in which there are expected to be thousands of planets found. Finding a system of n_p planets requires fitting of a total $5 + 7n_\mathrm{p}$ parameters: five astrometric and seven Keplerian parameters for every planet. The problem is thus highly non-linear and computationally prohibitive. After exploiting the linear properties of the Thiele-Innes constants, the remaining three non-linear parameters still limit the number of stars in the Gaia data that are practicable to probe for planets. The aim of this thesis is to investigate the feasibility of further eliminating two non-linear parameters, which is accomplished by assuming a circular orbit in the fit. If this approach is successful at reliably finding planet candidates even for eccentric orbits, it can possibly be used to expand the number of stars that can be searched for planets in the Gaia data. The approach is tested in simulated Gaia observations of known single- and multiple-planet systems from radial velocity (RV) measurements. Two detection metrics are used to enable comparison with past studies: a simple signal-to-noise (S/N) threshold and a more robust metric based on orbit fitting, the $\Delta\chi^2$ metric. The results indicate that, assuming a circular orbit in the fit, the orbital period can be correctly determined for planets with eccentricity $\lesssim 0.8$ in single-planet systems, and $\lesssim 0.5$ in multiple-planet systems. It is also found that around one third of the total number of planets in the current RV catalog, and at least one sixth of its multiple-planet system members, can reliably or somewhat reliably be detected and characterized by Gaia.

Populärvetenskaplig beskrivning

När Tycho Brahe på 1500-talet stod i sin Stjärneborg på ön Ven utanför Landskrona och kartlagde stjärnhimlens rörelser utövade han vad vi i dag kallar för astrometri: att mäta himlakropparnas positioner och rörelser. I ett historiskt skede skulle precisionen i Tychos mätningar komma att knyta ihop astronomin med fysik för första gången. Johannes Kepler, Tychos medhjälpare och efterträdare, kunde med hjälp av Tychos data räkna ut planeternas omloppsbanor kring solen och till slut generalisera dessa till vad som i dag fortsätter vara grundstenarna i den celesta mekaniken, nämligen Keplers lagar. Dessa lagar kom sedan att förklaras av Newtons gravitationslag, varvid astrofysiken såg dagens ljus. Utan tvekan var Tychos noggranna iakttagelser ett viktigt tillskott i denna historiska händelseföljd.

I december 2013 skickades den europeiska satelliten Gaia upp, som med sin utomordentliga precision kommer att observera närmare en miljard stjärnor och, likt Tycho, kartlägga deras positioner och rörelser. Precisionen av Gaia är sådan att den hade från Ven kunnat mäta vidden av ett hårstrå som befinner sig i Sundsvall! Detta möjliggör mätningar av de små störningar som Newtons lagar förutsäger att en planet utövar på sin värdstjärna, som förenat med den vida kartläggningen kommer att leda till många nya planetupptäckter. Det har uppskattats att Gaia under sina fem aktiva år kommer att finna och bestämma egenskaperna hos mer än 20 000 större planeter kring många olika typer av stjärnor.

Ett av problemen för de som jobbar med att skönja planetsignaler ur Gaias data är att det skulle krävas en oerhörd mängd datorkraft om man skulle söka igenom varje en av de miljarder stjärnor Gaia kollar på. Eftersom det inte är praktiskt möjligt, får man istället nöja sig med att söka igenom några av de miljoner stjärnor som man beräknar ha störst sannolikhet att härbärgera planeter. Därför vill man hitta genvägar som gör det möjligt att snabbare upptäcka planetkandidater och således också möjligt att söka igenom fler stjärnor. I denna uppsats görs ett försök att, genom en synbart enkel taktik, hitta en sådan genväg. I algoritmerna som söker efter planeter behöver man i regel ta hänsyn till alla egenskaper hos den omloppsbana man försöker bestämma. Taktiken i denna uppsats är att anta att banan är cirkulär istället för elliptisk. Eftersom en ellips kan se ut på ofantligt många fler sätt än en cirkel blir problemet på detta vis många gånger enklare. Om denna taktik visar sig fungera väl, skulle den kunna göra det praktiskt möjligt att leta efter planetkandidater i ännu fler av stjärnorna i Gaias data.

Om Gaia kommer att sätta avtryck i historien återstår att se, men klart är att satelliten, för planetforskningens räkning, kommer att generera en hel del data för ett rikt omfång av planetomgivna stjärnor. Detta kommer att ge oss insikter i fördelningen och egenskaperna av de större planeterna som bland annat kan användas för att testa olika teorier om planetbildning. I vilket fall som helst fortsätter Gaia Tychos tradition att kartlägga himlen med oöverträffad precision, vilket, i ett historiskt perspektiv, kan ha oförutsägbara följder.

Contents

Chapter 1

Introduction

The inventory of exoplanets detected by astrometry is currently populated by zero objects. This number reflects the inherent difficulty of the technique, which derives from the exceedingly small astrometric effect a planet has on its host star. Despite this difficulty, the principles of planet detection by astrometry have frequently been applied throughout history. One of its earliest pioneers was Erik Holmberg, who, working from Lund Observatory, reported that Proxima Centauri had a companion with a mass "only some few times larger than the mass of Jupiter" (Holmberg, 1938). It was later realized, however, that the instruments he used were not sensitive enough and that the suspected signal was likely just noise (Perryman, 2011). Some decades later, in what is probably the most (in)famous astrometric planet detection, van de Kamp (1963) announced a companion with about 1.6 times the mass of Jupiter orbiting the nearby Barnard's star. The Barnard's star companion was initially accepted by the astronomy community and even featured in textbooks as the first exoplanet discovery (Livio et al., 2011). Nevertheless, what van de Kamp saw in his 25 years of data was soon identified as a probable systematic error and the observation could not be reproduced by others. There are more examples of claimed astrometric detections (see, e.g., Sozzetti (2010), and references therein), some of which still await confirmation[1], but most have not survived scrutiny. Instead, the first detected, and still recognized, planet around a Sun-like star came in 1995 from radial velocity (henceforth RV) measurements (Mayor & Queloz, 1995). Most of the subsequent ∼1900 confirmed[2] exoplanets have been detected by the RV and photometric transit methods, with a few by direct imaging, pulsar timing and gravitational lensing techniques. However, the December 2013 launch of the European Space Agency's (ESA) satellite *Gaia* is likely to turn the tide for planet detection by astrometry. During its five-year astrometric all-sky survey mission of nearly one billion stars, it is estimated that Gaia will detect and characterize some

---

[1] An astrometric detection of a planet in the binary system HD 176051 was recently claimed by Muterspaugh et al. (2010).

[2] As of May 15, 2015, the total number of confirmed planets in the Extrasolar Planets Encyclopaedia (`exoplanet.eu`) is 1921, whereas the slightly more conservative Exoplanet Orbit Database (`exoplanets.org`) lists 1523.

20 000 high-mass (1–15 M_J) planets in long-period orbits around a wide variety of host stars (Perryman et al., 2014), and in the process provide some important missing pieces of the current exoplanet catalog.

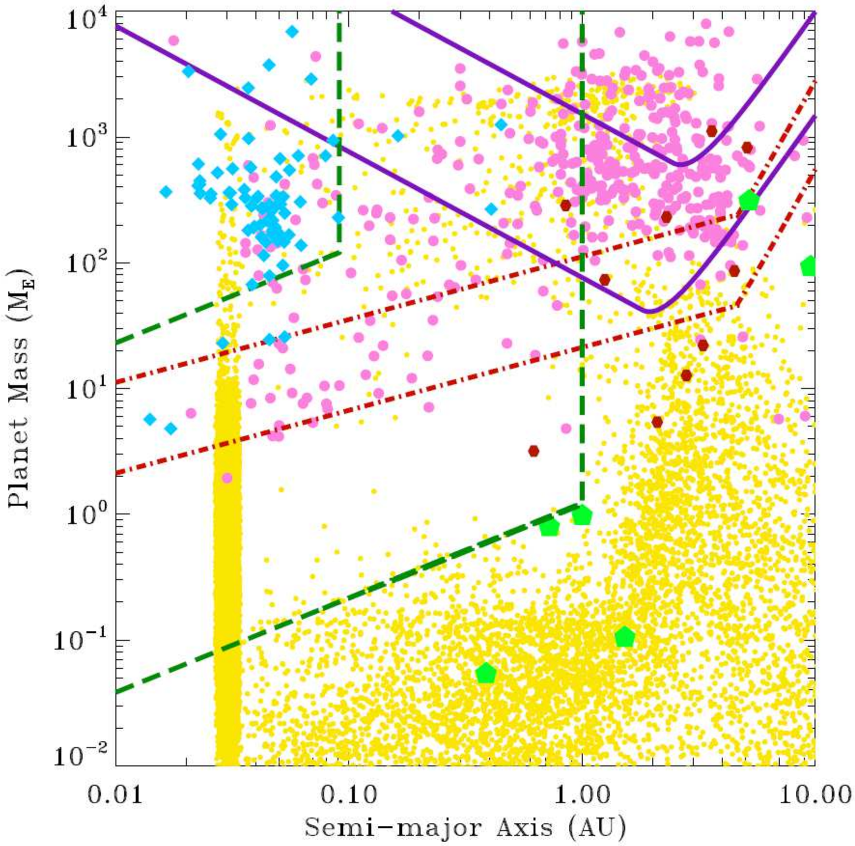

Figure 1.1: The Gaia exoplanet discovery space compared to the RV and transit methods, based on a S/N = 3 threshold. The upper and lower Gaia curves (purple lines) show detectability of a 5-year mission with $\sigma_{\text{fov}} = 10$ µas for a 1 $M_\odot$ star at 200 pc and a 0.4 $M_\odot$ star at 25 pc, respectively. The upper and lower RV curves (red dash-dotted lines) assume $\sigma_{\text{RV}} = 3\ \mathrm{m\,s^{-1}}$ and $1\ \mathrm{m\,s^{-1}}$, respectively. The upper and lower transit curves (green dashed lines) assume $\sigma_V = 5$ mmag and 10 µmag, respectively. Symbols show inventory (as of May 2010) of RV-detected planets (pink circles), transiting systems (light-blue diamonds) and planets detected by microlensing (red hexagons). The green filled pentagons are solar system planets and the small yellow dots show a theoretically predicted distribution of planets (Ida & Lin, 2008). Figure from Sozzetti (2011).

There are a number of key advantages to using astrometry to detect planets. In addition to supplying almost complete information on the orbital parameters (see Section 2.3), astrometry is sensitive in slightly different areas compared to other methods. In general, astrometric sensitivity increases with the mass and semi-major axis (and thus orbital period) of the planet, which can constitute a meaningful complement to the current catalog. The Gaia exoplanet discovery space compared to various other methods is shown in Figure 1.1. The contribution from Gaia may not seem very noteworthy if the discovery space is considered only in isolation; a more nuanced view of the prospect is considering the context of an all-sky survey that is limited almost solely by the magnitude of the host star, that will also provide accurate measurements of the stellar parameters such as luminosity, distance, metallicity, spectral type and age of the star. Thus, Gaia will provide not only improved constraints to already known systems, but will yield an abundance of new planets around stars of all types. Notably, Gaia will provide unprecedented statistics of the giant planets, with highly accurate information on their variability as a function of stellar parameters (Sozzetti, 2010). Furthermore, by having access to the orbital inclination, i, the unique mass of the planet, M_p, can be determined, in contrast to RV measurements, which only yield the minimum mass of the planet, $M_\mathrm{p} \sin i$. For a small, but not insignificant, number of multiple-planet systems, Gaia can also provide measurements of the co-planarity, a largely unexplored parameter in exoplanetary science (Casertano et al., 2008), that will inform the models of planetary formation and evolution.

Searching for planetary signals in the vast amounts of astrometric data produced by Gaia will be a computational challenge. For a system of n_p planets, the total number of parameters to be fitted algorithmically is $5 + 7n_\mathrm{p}$, which can require substantial computational resources, especially for systems with many planets. Of the around one billion stars that Gaia will observe, only millions can practically be expected to be thoroughly inspected for planets, which necessitates high efficiency in the algorithms. The problem can be mitigated somewhat by drawing on the linearity of $5 + 4n_\mathrm{p}$ of the parameters, leaving $3n_\mathrm{p}$ non-linear parameters to be fitted (Wright & Howard, 2009). The aim of this thesis is to evaluate the feasibility of removing two additional non-linear parameters, accomplished by assuming a circular orbit in the fit. This effectively limits the search to a range of orbital periods and, if successful, makes the algorithm more efficient at finding planet candidates. The approach can potentially be used to increase the total number of stars in the Gaia data that are practicable to probe for planets. This more efficient algorithm can later supply the most promising planet candidates as starting points for more sophisticated algorithms. The approach is tested on simulated Gaia observations of real single- and multiple-planet systems known from RV measurements. An orbit-fitting algorithm assuming a circular orbit is applied to each planet, one at a time, in a blind search for the orbital period. Two distinct investigations are conducted: an *individual* orbit-fitting scheme to all (436) RV planets[3] with no distinction made between members of single- and multiple-planet systems, and a *composite* orbit-fitting scheme to the (55) RV multiple-planet systems, where the combined signal of all planets is searched and the signal of the first fit is removed before searching for the next, etc. Further, the detectability of the planets is estimated by two different metrics: a simple signal-to-noise ratio (S/N), easily comparable to past studies, and a more robust metric based on statistical properties

---

[3] Their data taken from `exoplanets.org`.

of the orbit-fitting, the $\Delta\chi^2$ metric, as utilized by Perryman et al. (2014).

This text is organized as follows. Chapter 2 introduces astrometry as planet detection and characterization tool, wherein Section 2.1 describes the main observable in astrometric planet detection, the astrometric signature; Section 2.2 describes the astrometric and Keplerian parameters and to what extent the latter are available to astrometry; Section 2.3 provides the theoretical background for the modeling and fitting of a star-planet system; and Section 2.4 describes the two detectability metrics used in the investigations. Chapter 3 describes the methods used in this thesis, wherein Section 3.1 describes an empirical determination of the $\Delta\chi^2$ threshold values; Section 3.2 gives a description of the Gaia observation simulations and how the modeling of the star-planet systems is done; and Section 3.3 gives a detailed description of the orbit-fitting algorithm used in the investigations. The results of the experiments are showcased in Chapter 4. Finally, Chapter 5 provides a discussion of the results, a brief overview of the prospects of astrometry in exoplanetary science and some concluding remarks.

Chapter 2

Exoplanet detection using astrometry

2.1 The astrometric signature

Planet detection with astrometry is an indirect method, meaning that it does not directly observe the photons of planets around other stars. Rather, the existence of the planet is inferred by measuring the minute transversal components of the *reflex motion* of the host star. The reflex motion is due to the gravitational pull from the orbiting planet and is described by an ellipse with one of its foci at the barycenter (center of mass) of the star-planet system. The semi-major axis of the star is

$$a_* = \left(\frac{M_\mathrm{p}}{M_\mathrm{p} + M_*}\right) a_\mathrm{p} \simeq \left(\frac{M_\mathrm{p}}{M_*}\right) a_\mathrm{p}\,, \tag{2.1}$$

where M_* is the mass of the star, M_p and a_p the mass and semi-major axis of the planet, respectively (the last approximation holds since $M_\mathrm{p} \ll M_*$). Since a_* is likely to be measured in angular units[1], the observable for planetary detection, the *astrometric signature*, is defined as (Perryman, 2011)

$$\alpha \equiv \left(\frac{a_*}{1\ \mathrm{AU}}\right)\left(\frac{d}{1\ \mathrm{pc}}\right)^{-1} \simeq \left(\frac{M_\mathrm{p}}{M_*}\right)\left(\frac{a_\mathrm{p}}{1\ \mathrm{AU}}\right)\left(\frac{d}{1\ \mathrm{pc}}\right)^{-1} \mathrm{as} \tag{2.2}$$

where d is the distance to the star. It is clear that α increases with the period of the planet, P, due to Kepler's third law, where $P^2 \propto a_\mathrm{p}^3$. Moreover, α increases with the mass of the planet while it decreases with the distance to the system. Therefore, astrometry favors the detection of long-period, high-mass planets in nearby systems. An illustrative example of the size of the effect is that for an Earth-mass planet orbiting a Sun-like star at 1 AU, $\alpha \simeq 3d^{-1}$ µas. Earth-mass planet signals are thus too small to be detected by Gaia

---

[1] One degree (°) equals 60 arcminutes, or 3600 arcseconds (as). One milliarcsecond (mas) equals 0.001 arcseconds and one microarcsecond (µas) equals 0.001 mas.

(see Section 2.4) but could be by future missions (see Chapter 5). On the other hand, for a planet with the mass and orbit of Jupiter, $\alpha \simeq 5d^{-1}$ mas, which is readily detectable by Gaia out to $d \simeq 50$ pc.

2.2 The astrometric and Keplerian parameters

Astrometry is generally concerned with measuring the position and motion of objects on the celestial sphere relative to some coordinate system, most commonly the equatorial system[2]. The position and motion of a star without orbiting companions can be described by the five *astrometric parameters*: right ascension, α_0, and declination, δ_0, at some reference epoch t_0; the parallax, ϖ, due to the observer's orbital motion; and the transversal proper motions, $\mu_{\alpha*}$ and μ_δ,[3] in right ascension and declination, respectively. The observed path of a star with uniform space motion can thus be modeled as

$$\begin{aligned}\Delta\alpha_*(t) &= \Delta\alpha_{0*} + \Pi_\alpha(t)\varpi + (t-t_0)\mu_{\alpha_*}\\ \Delta\delta(t) &= \Delta\delta_0 + \Pi_\delta(t)\varpi + (t-t_0)\mu_\delta \ ,\end{aligned} \tag{2.3}$$

where $\Delta\alpha_{0*}$ and $\Delta\delta_0$ are the astrometric displacements (the difference from the true position and the position at reference epoch t_0) and Π is a factor mapping the orthogonal components of the parallax, given as (Perryman, 2011)

$$\begin{aligned}\Pi_\alpha(t) &= r_x(t)\sin\alpha - r_y(t)\cos\alpha\\ \Pi_\delta(t) &= [r_x(t)\cos\alpha + r_y(t)\sin\alpha]\sin\delta - r_z(t)\cos\delta \ ,\end{aligned} \tag{2.4}$$

where (r_x, r_y, r_z) are the cartesian components of the position of the observatory[4].

The three-dimensional orbit of a planet around a star is described by the seven *Keplerian parameters*: $a_\mathrm{p}, e, P, t_\mathrm{p}, i, \Omega, \omega$ (see Figure 2.1). The semi-major axis of the planet, a_p, is measured with respect to the host star; e is the eccentricity; P is the orbital period; t_p is the time of periapsis, a point in time when the planet is closest to the host star. The last three angular parameters are completely dependent on the position of the observer:

---

[2] In the equatorial system, the fundamental plane is the plane projected from the Earth's equator with a primary direction defined at the point where the path of the Sun intersects the equatorial plane going from south to north (the Sun's longitude of the ascending node, see below). Because the equatorial and ecliptic planes are moving due to precession and nutation, a reference epoch, e.g., J2000.0, has to be specified for every set of equatorial coordinates (α, δ).

[3] Since the nominal right ascension is measured along the equator (where $\delta = 0$), the actual coordinate needs to be given in great circle measure, written as $\alpha_* \equiv \alpha\cos\delta$. Thus $\mu_{\alpha*} = \mu_\alpha\cos\delta$.

[4] The values for Π can be obtained from the NASA JPL Solar System ephemerides (Seidelmann, 1992), but for space-borne high-precision astrometry observatories such as Gaia, they have to be computed using the precise location of the spacecraft, measured by telescopes on the ground.

the inclination, i, is the angle of the orbital plane to the tangential plane of the celestial sphere; the longitude of the ascending node, Ω, is the point where the orbit of the planet moves away (as seen from the observer) from the tangential plane; and the argument of periapsis, ω, is the node of closest approach to the host star, measured from the ascending node.

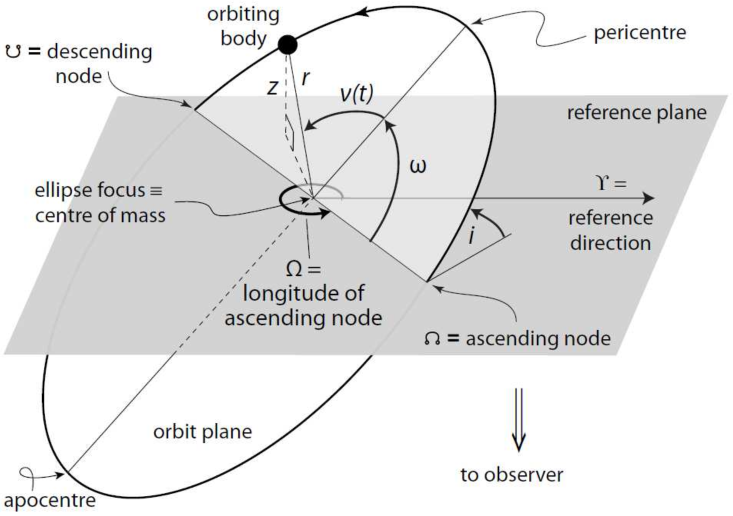

Figure 2.1: The Keplerian parameters of a body orbiting the barycenter. See text for explanation. Figure from Perryman (2011).

A common way to characterize the elliptical orbit of a planet is by defining the true anomaly, $v(t)$, as the angle to the planet at a time t, as seen from the system barycenter and measured from the argument of periapsis, ω (see Figure 2.1). The true anomaly is calculated by first defining the eccentric anomaly, $E(t)$, which is the angle to the planet if it were to trace an auxiliary circle with a radius equal to the semi-major axis of the orbital ellipse, measured from the center of the ellipse, starting at t_p. The geometric relation between the true and eccentric anomalies can be expressed (Perryman, 2011)

$$\cos v(t) = \frac{\cos E(t) - e}{1 - e\cos E(t)}\,. \tag{2.5}$$

Moreover, the orbital frequency $f \equiv 1/P$, associated with the mean motion of the planet around the barycenter, is used to define the mean anomaly, a fictitious angle traced by the planet since the last time of periapsis, t_p:

$$M(t) = 2\pi f(t - t_\mathrm{p}) = M_0 + 2\pi f(t - t_0)\,. \tag{2.6}$$

As can be seen in Equation (2.6), the mean anomaly can also be measured from M_0, which is M at a reference epoch t_0 and takes on a value 0–360°. M_0 can thus be used as a substitute for the Keplerian parameter t_p (which is done from here on). The mean anomaly can then be used to calculate the true anomaly by iteratively solving Kepler's equation

$$E(t) - e \sin E(t) = M_0 + 2\pi f(t - t_0)\,. \tag{2.7}$$

All of the seven Keplerian parameters can in principle be determined by orbit-fitting to astrometric data, with the exception that astrometric measurements yield no information about which of the nodes is ascending (Perryman et al., 2014). Further, a_* can be determined from α (Equation (2.2)), given that the distance, d, is known (which can be measured directly by astrometry for parallax stars). Importantly, and in contrast to RV measurements, full astrometric orbit solutions give i (Perryman et al., 2014), which can be used to determine the unique mass of the planet with Equation (2.1), assuming $M_\mathrm{p} \ll M_*$ and that M_* is known from, e.g., spectral type or evolutionary models.

2.3 Joint modeling of the astrometric and Keplerian parameters

The Keplerian parameters in the reflex motion of the star are identical to those of the planet, except for the semi-major axis, a_*, which differs by a factor M_p/M_* (Equation (2.1)), and the argument of periapsis, ω_*, which is directly opposite to that of the planet, i.e., $\omega = \omega_* + \pi$. Consequently, four of the seven Keplerian parameters can be re-cast as the so-called Thiele-Innes constants (see Binnendijk (1960) for a derivation):

$$\begin{aligned}
A &= a_*(+\cos\omega_* \cos\Omega - \sin\omega_* \sin\Omega \cos i)\\
B &= a_*(+\cos\omega_* \sin\Omega + \sin\omega_* \cos\Omega \cos i)\\
F &= a_*(-\sin\omega_* \cos\Omega - \cos\omega_* \sin\Omega \cos i)\\
G &= a_*(-\sin\omega_* \sin\Omega + \cos\omega_* \cos\Omega \cos i)\,.
\end{aligned} \tag{2.8}$$

These constants are particularly useful in an orbit-fitting scheme, since they linearize four of the seven parameters, making the problem more tractable for computation.

The barycenter motion of a star with n_p planets can be modeled by introducing the Keplerian parameters as perturbations to the purely astrometric motion described by Equation (2.3), such that (Wright & Howard, 2009)

$$\begin{aligned}
\Delta\alpha_*(t) &= \Delta\alpha_{0*} + \Pi_\alpha(t)\varpi + (t - t_0)\mu_{\alpha*} + \sum_{i=1}^{n_\mathrm{p}} \left[B_i X_i(t) + G_i Y_i(t)\right]\\
\Delta\delta(t) &= \Delta\delta_0 + \Pi_\delta(t)\varpi + (t - t_0)\mu_\delta + \sum_{i=1}^{n_\mathrm{p}} \left[A_i X_i(t) + F_i Y_i(t)\right]\,,
\end{aligned} \tag{2.9}$$

where X and Y are the displacements in elliptical rectangular coordinates, defined as

$$\begin{aligned} X(t) &= \cos E(t) - e \\ Y(t) &= \sqrt{1-e^2}\,\sin E(t)\,. \end{aligned} \tag{2.10}$$

The eccentric anomaly E is calculated iteratively with Equation (2.7). With the use of the Thiele-Innes constants, only X and Y contain non-linear parameters in Equation (2.9) and the problem is now only non-linear with respect to e, M_0 and f and is thus manageable for an orbit-fitting algorithm. An algorithm to determine the parameters can, e.g., perform a simultaneous linear least-squares fit of the combined displacement from the astrometric and Keplerian parameters. The best-fitting parameters are then determined by a minimization of the chi-squared statistic, given by

$$\chi^2 \equiv \sum_i \left(\frac{r_i}{\sigma_i}\right)^2 \tag{2.11}$$

where r is the residuals of the fit and σ the uncertainty of the measurement (the along-scan uncertainty per field of view crossing, $\sigma_{\rm fov}$, see Section 2.4). Such a linear least-squares fitting procedure is detailed in Section 3.3.

2.4 Detectability estimation

In simulations estimating the detectability of planets, good knowledge of the expected measurement uncertainty is required. For the purposes of this investigation, only instrumental uncertainties are considered. Other noise sources, such as stellar jitter and relativistic effects are either negligible or can be calculated accurately and thus accounted for. The Gaia along-scan uncertainty per field of view crossing is given by (Perryman et al., 2014)

$$\sigma_{\rm fov} = \left(\frac{\sigma_\eta^2}{9} + \sigma_{\rm att}^2 + \sigma_{\rm cal}^2\right)^{0.5} \tag{2.12}$$

where $\sigma_{\rm att}$ and $\sigma_{\rm cal}$ are the uncertainties of the attitude of the spacecraft and the calibration, respectively, both estimated around 20 µas. The centroiding uncertainty of the nine Charged Coupling Devices (CCD), σ_η, is dependent on the magnitude[5] of the observed object. The values of σ_η and $\sigma_{\rm fov}$ are shown in Table 2.1.

---

[5] Gaia observes in the so-called G magnitude band, with the wavelength coverage ~330–1050 nm (see `http://www.cosmos.esa.int/web/gaia/science-performance`), which, for the purposes of this investigation, can be taken to be equal to the visual magnitude band V (centered around 555 nm).

Table 2.1: The Gaia CCD centroiding uncertainty, σ_η, and along-scan uncertainty per field of view crossing, σ_{fov}, as a function of G ($\simeq V$) magnitude. Most of the host stars in the RV sample used in this investigation have magnitudes $V < 12$. Values from Table 2 in Perryman et al., 2014.

G (mag)	σ_η (µas)	σ_{fov} (µas)
6–12	57.8	34.2
13	91.7	41.6
14	145.4	56.1
15	230.9	82
16	367.5	125.7
17	588.9	198.3
18	958.1	320.6
19	1612.8	538.4
20	2898.3	966.5

With knowledge of the measurement uncertainty, a zeroth-order estimation of the planet detectability is the signal-to-noise ratio

$$\text{S/N} \equiv \alpha/\sigma_{\text{fov}}\,. \tag{2.13}$$

The S/N has been used, e.g., to show that the orbits of planets with a S/N > 3 (and P less than the mission lifetime) can reliably and consistently be determined by Gaia (Casertano et al., 2008). The fact that it has been used in past studies and that it does not rely on detailed simulations make the S/N practical and useful as a comparison with past estimates. However, the S/N does not take into account important factors that affect the detectability, such as the inclination and eccentricity of the orbit and the number and distribution of observations. This shortcoming is especially relevant since the all-sky survey of Gaia follows a scanning law that does not provide a homogeneous temporal and spatial covering of the whole celestial sphere (see Figure 2.2). Furthermore, the S/N requires knowledge of the orbital parameters of the planet, which does not make it applicable to real data.

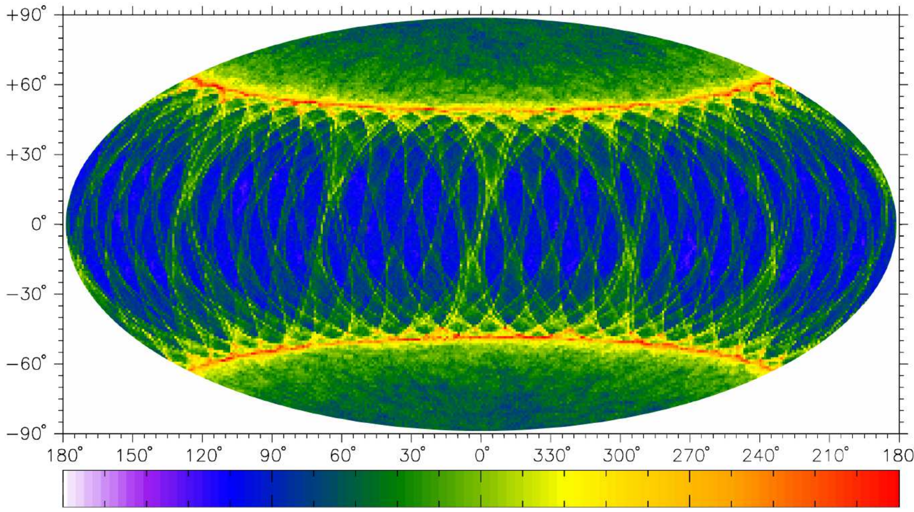

Figure 2.2: The Gaia nominal scanning law in Hammer-Aitoff projection of the whole sky. The 0° on the vertical axis corresponds to the plane of the ecliptic. The color bar indicates the number of field of view crossings, going linearly from 0 (white) to 200 (red). After accounting for dead time (unplanned spacecraft outages, data loss etc.), the average number of crossings over the 5-year mission lifetime is 70. Figure and data from de Bruijne (2012).

An improved measure of detectability is therefore one that can take the Gaia nominal scanning law into account, along with the relevant orbital parameters of the system. One such measure is the $\Delta\chi^2$ metric, which is based on the statistical properties of orbit-fitting (Perryman et al., 2014). It works by comparing the best value of the goodness-of-fit of a 12 parameter (astrometric and Keplerian) model for a star with planetary perturbations, $\chi^2_{\text{min},12}$, to the best goodness-of-fit of a five parameter (astrometric) model fitted to the same star without any planetary perturbations, $\chi^2_{\text{min},5}$. Hence, $\chi^2_{\text{min},5} \geq \chi^2_{\text{min},12}$ and the increase in χ^2 when going from the 12 parameter to the five parameter fit is

$$\Delta\chi^2 \equiv \chi^2_{\text{min},5} - \chi^2_{\text{min},12} \,. \tag{2.14}$$

The $\Delta\chi^2$ can be shown (done empirically in Section 3.1) to be related to the likelihood ratio of the models and can thus be used as a measure of the significance of the orbit. A $\Delta\chi^2(f)$ spectrum of the searched frequencies in the orbit-fitting algorithm can be obtained, which is then similar to a Lomb-Scargle normalized periodogram[6], a commonly used tool to detect and gauge the false-alarm probability of a signal in unevenly spaced time series (see, e.g., Section 13.8 in Press et al., 2007). For the present purposes of assuming $e = 0$ in the orbital fit, there is no longer any point of periapsis, which makes ω largely meaningless and Equations (2.7) and (2.5) give $M(t) = E(t) = v(t)$. Consequently, there are three Keplerian parameters no longer in the linear fit and the 12 parameter fit above effectively reduces to a nine parameter fit, explaining the notation χ^2_9 used in Section 3.3.

---

[6] A diagram with spectral power as a function of f, despite having the word 'period' in the name.

Chapter 3

Methods

There are two distinct investigations conducted in this thesis: a) *individual* orbit-fitting to all (436) RV planets with no distinction made between members of single- and multiple-planet systems, b) *composite* orbit-fitting to the (55) RV multiple-planet systems, where the combined signal of all planets is searched and the signal of the first fit is removed before searching for the next, etc. In this chapter, the methods used in both investigations are explained in parallel with their variations highlighted throughout. Preceding the description of the orbit-fitting procedure is a description of an empirical determination of the $\Delta\chi^2$ detection threshold, then followed by an explanation of the underlying Gaia simulations and how the model for a star with orbiting companions can be combined with them.

3.1 Determining the $\Delta\chi^2$ detection threshold

Before doing any simulations to determine the detectability, a threshold value for what counts as a reliable detection is needed. That $\Delta\chi^2$ is related to the likelihood ratio of the models can be "proved" by repeatedly fitting the orbit-fitting algorithm to nothing but the Gaussian noise used in the investigations, which will sometimes yield peaks with high values of $\Delta\chi^2$ merely by chance. Thus, a search for the occurrence of these peaks over a very high number of experiments enables an empirical determination of the probability, p, of obtaining a given value of $\Delta\chi^2$ from just noise. The value of p is called the *significance level* of the peak, which thus describes the false-alarm probability for a given value of $\Delta\chi^2$. That is, a large value of $\Delta\chi^2$ corresponds to a small value of p and a highly significant orbit.

To determine the significance levels, the orbit-fitting algorithm (Section 3.3) is run with no signal for 10 000 experiments, each over a random direction in the sky (determined by picking the direction of the host star of a random planet in the RV sample) and with a different Gaussian noise realization (the standard deviation of which, σ_{fov}, is determined by the magnitude of the selected host star). Thus, the point of maximum $\Delta\chi^2$ above which there are, including itself, $10\,000 \times p$ points, corresponds to the respective significance level p. So, in a diagram, there will be a total of, e.g., $10\,000 \times 0.0005 = 5$ points above a certain value of $\Delta\chi^2$, which is then taken to correspond to $p = 0.0005$. Such a diagram with the resulting $\Delta\chi^2$ for all p-values is shown in Figure 3.1.

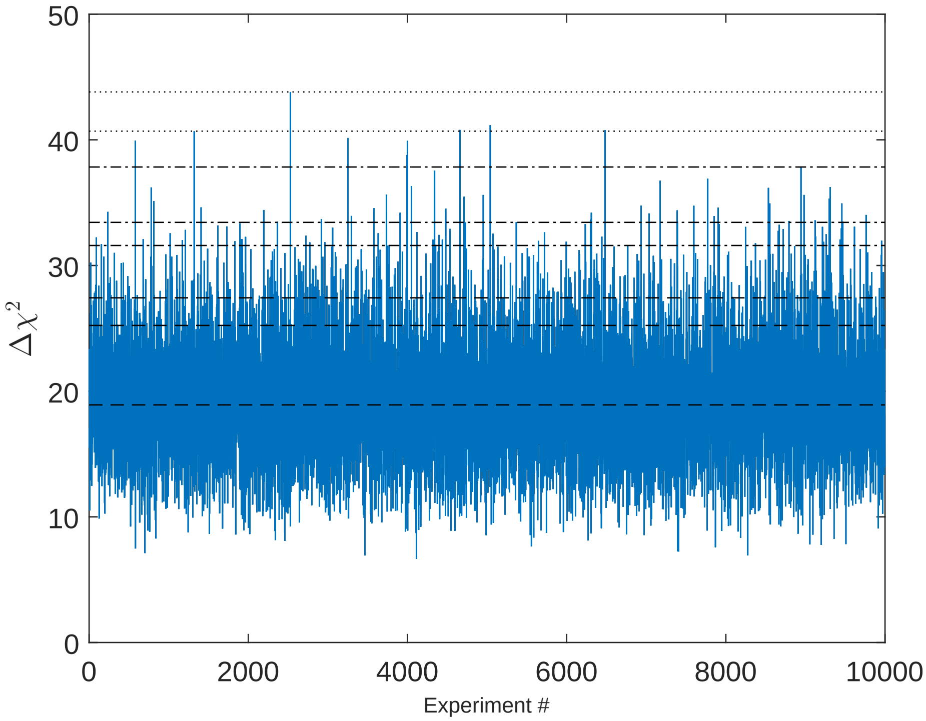

p	$\Delta\chi^2$
0.0001	43.8
0.0005	40.7
0.001	37.8
0.005	33.4
0.01	31.6
0.05	27.4
0.1	25.2
0.5	18.9

Figure 3.1: The periodogram for the test to determine the $\Delta\chi^2$ detectability threshold. The significance levels, the values of $\Delta\chi^2$ corresponding to p, are denoted by the horizontal lines in the diagram. The numeric values of the empirical $\Delta\chi^2$ are shown in the table to the right.

3.2 Modeling a star-planet system with simulated Gaia observations

Realistic simulations of the Gaia observations are obtained from the software package AGISLab (Holl et al., 2012; their Appendix B). For the present purposes, AGISLab provides a simulated five-year Gaia experiment over 48 different directions[1] on the celestial sphere, based on the nominal scanning law (Figure 2.2). For a star in any given direction, AGISLab has computed a list including the expected number of crossings, n, of the star over the Gaia along-scan field during one experiment; the measurement epoch, t; the position angle of the scan, θ; and the parallax factor of each crossing due to the spacecraft, Π_η.

The stellar image in the Gaia field of view is transformed into the along-scan field angle η, as shown in Figure 3.2, such that

$$\Delta\eta = \Delta\alpha_* \sin\theta + \Delta\delta\cos\theta\,. \tag{3.1}$$

The displacement due to the five astrometric parameters for a measurement epoch i is then modeled as

$$\Delta\eta_{5,i} = \frac{\partial\eta_i}{\partial\alpha_*}\Delta\alpha_* + \frac{\partial\eta_i}{\partial\delta}\Delta\delta + \frac{\partial\eta_i}{\partial\varpi}\varpi + \frac{\partial\eta_i}{\partial\mu_{\alpha*}}\mu_{\alpha*} + \frac{\partial\eta_i}{\partial\mu_\delta}\mu_\delta \tag{3.2}$$

where the partial derivative $\frac{\partial\eta}{\partial p_k}$ describes the contribution of the parameter p_k. The values of the partial derivatives at each measurement epoch are calculated by AGISLab using the along-scan position angle θ of the Gaia field of view and the associated parallax is calculated using the position of the spacecraft (Equation (2.4)). The relations are

$$\frac{\partial\eta}{\partial\alpha_*} = \sin\theta\,, \qquad \frac{\partial\eta}{\partial\delta} = \cos\theta\,,$$

$$\frac{\partial\eta}{\partial\mu_{\alpha*}} = \Delta t\sin\theta\,, \qquad \frac{\partial\eta}{\partial\mu_\delta} = \Delta t\cos\theta\,, \tag{3.3}$$

$$\text{and} \qquad \frac{\partial\eta}{\partial\varpi} \;=\; \Pi_\alpha\sin\theta + \Pi_\delta\cos\theta \;=\; \Pi_\eta\,,$$

where $\Delta t = t - t_0$ and $t_0 = 2017.0$ a reference epoch set at approximately mid-mission. The displacement (Equation (3.2)) can thus be written as

$$\Delta\eta_{5,i} = [\Delta\alpha_* + \mu_{\alpha*}\Delta t_i]\sin\theta_i + \Pi_{\eta,i}\varpi + [\Delta\delta + \mu_\delta\Delta t_i]\cos\theta_i\,. \tag{3.4}$$

---

[1] In this particular simulation, the celestial sphere is divided into 48 equiareal pixels, called a Hierarchical Equal Area isoLatitude Pixelization (HEALPix), where each pixel center represents a direction. The celestial sphere can in general be divided into 3×4^m pixels, for any integer $m \geq 1$. See `http://healpix.jpl.nasa.gov/`.

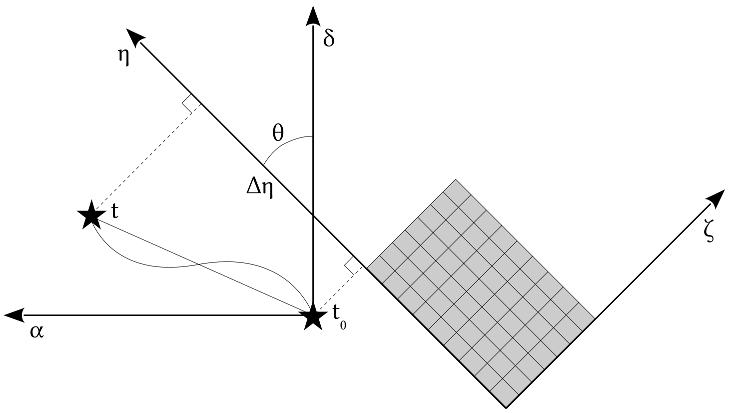

Figure 3.2: Gaia's astrometric field CCDs (gridded gray area) scans along the direction η. The along-scan position angle, θ, is used to transform the motion of the star in the stellar frame (α, δ) to the astrometric field frame (η, ζ), where the motion of the star from t_0 to t is represented by $\Delta\eta$.

To model the perturbations from a planet, the linear Thiele-Innes constants from Equation (2.9) are introduced. The displacement of the stellar image due to the seven Keplerian parameters is then

$$\Delta\eta_{7,i} = [B_i X_i + G_i Y_i] \sin\theta_i + [A_i X_i + F_i Y_i] \cos\theta_i \,, \tag{3.5}$$

where X and Y are from Equation (2.10), respectively, containing the non-linear parameters e and E, which are calculated by iteratively solving Equation (2.7).

The total displacement of the stellar image due to the astrometric and Keplerian parameters is the sum of Equations (3.4) and (3.5):

$$\Delta\eta_i = \Delta\eta_{5,i} + \Delta\eta_{7,i} \,. \tag{3.6}$$

Finally, to simulate an observation of the total stellar displacement, a noise term, ν_i, containing independent, normally distributed noise over all measurement epochs and with standard deviation σ_{fov}, is added. The simulated observation of the total displacement at measurement epoch i is thus

$$\Delta\eta_i^{\mathrm{obs}} = \Delta\eta_i + \nu_i \,. \tag{3.7}$$

3.3 The orbit-fitting procedure for single- and multiple-planet systems

In this section, one *experiment* for a single- or multiple-planet system is described in a step-by-step fashion. The experiment includes simulating 5 years of Gaia observations and applying a linear least-squares orbit-fitting routine. Subsequently, the detectability metrics $\Delta\chi^2$ and S/N are calculated. The general procedure is similar for the single and multiple-planet cases, with some crucial differences in the latter case, noted at the end of the affected steps.

Before the modeled star-planet systems are put into the Gaia observation simulations, some initial considerations and motivations are necessary. From the RV planet data, four of the Keplerian parameters are known: e, ω, a_{p} and $f_{\mathrm{true}} = 1/P$. The remaining three parameters, Ω, M_0 and i, are assumed unknown[2] and thus have to be simulated. Ω and M_0 assume for each experiment a random value between 0° and 360°. Moreover, four different values of i are used, namely, 10°, 30°, 60° and 90°, where each is held constant for a set number of experiments (10). The variation in i is motivated by the two-fold effect it has on the detectability (see Figure 3.3): a) since only the minimum masses of the RV planets are known, i.e., $M_{\mathrm{p}} \propto 1/\sin i$, a smaller value of i gives a larger M_{p} and thus α (Equation (2.2)); b) a smaller angle i results in a larger projection of the orbit in the sky and thus permits a more complete observation of the orbital path. The effect a) has a considerable impact on the detectability, while b) is negligible in comparison. Further, a search in f, as opposed to P, is done because the resolution in f is largely independent of P, while in P it varies as P^2 (Perryman et al., 2014), which would result in a non-constant step-size. The step-size, $\Delta f = 0.01$ yr^{-1}, is empirically chosen such that an adequate sampling of the peaks in the $\Delta\chi^2$ periodogram is obtained, with about five points at the very top of an average-sized peak. The correct orbital frequency is then considered "found" when the best-fit frequency f_{fit} is within 0.05 yr^{-1} of f_{true}. The chosen range of searched frequencies (0.01–500 yr^{-1}) used in Step 5 is motivated by the range of frequencies in the RV planet data sample (0.07–496 yr^{-1}). The sampling of Gaia is highly irregular with an average sampling rate of 14 yr^{-1} (since the average number of crossings is 70) and a minimum separation of $\Delta t = 106.5$ min (due to the 6 hr spin period). Thus, the theoretical frequency for the sampling with minimum separation is $1/(2\Delta t) \simeq 2500$ yr^{-1} (the Nyquist frequency), which makes the upper limit of 500 yr^{-1} reasonable.

Input data

The data output from AGISLab is organized such that the simulated crossings ($t, \sin\theta$, $\cos\theta$ and Π_η) of each of the 48 directions are stored in 48 plain text files, in which each row corresponds to a measurement epoch t. An additional text file contains the coordinates of each of the directions and the name of the file containing the simulated crossings over that direction.

---

[2] For some planets in the sample, i may be known from transit measurements, but this is ignored.

The planet data is downloaded from `exoplanets.org/table` (filter `"PLANETDISCMETH == 'RV'"`) as a plain text file where each row is a planet with the following parameters: *planet name*, α_0, δ_0, M_* [$M_\odot$], d [pc], V, $M_\mathrm{p}\sin i$ [M_J], a_p [AU], P [d], ω [°], e.

Step 1. Load simulated crossings data

The parameters of the planet selected for simulation is loaded from the planet data file. To find which simulated crossings file to use, the angle $\phi = \cos^{-1}(\hat{\mathbf{u}}_* \cdot \hat{\mathbf{u}}_\mathrm{dir})$ between the unit vector of the star, $\hat{\mathbf{u}}_* = (\cos\alpha\cos\delta, \sin\alpha\cos\delta, \sin\delta)$, and the unit vector of each direction, $\hat{\mathbf{u}}_\mathrm{dir} = (\cos\alpha_h\cos\delta_h, \sin\alpha_h\cos\delta_h, \sin\delta_h)$ $(h = 1, \ldots, 48)$, is compared. The direction with the minimum ϕ is selected as the observing direction[3] and the corresponding crossings data are loaded into the matrix

$$\mathbf{M} = \begin{pmatrix} \sin\theta_1 & \cos\theta_1 & \Pi_{\eta,1} & \Delta t_1 \sin\theta_1 & \Delta t_1 \cos\theta_1 \\ \sin\theta_2 & \cos\theta_2 & \Pi_{\eta,2} & \Delta t_2 \sin\theta_2 & \Delta t_2 \cos\theta_2 \\ \vdots & \vdots & \vdots & \vdots & \vdots \\ \sin\theta_n & \cos\theta_n & \Pi_{\eta,n} & \Delta t_n \sin\theta_n & \Delta t_n \cos\theta_n \end{pmatrix}, \tag{3.8}$$

where n is the total number of crossings for the selected direction. The epochs of the crossings are stored in a vector $\mathbf{t} = (t_1, \ldots, t_n)$. To simulate the dead time (unplanned spacecraft outages, data loss etc.), a random subset of 15% of the crossings is removed from both $\mathbf{M}$ and $\mathbf{t}$.

Step 2. Astrometric displacement

The displacement due to the motion of the star can be calculated by creating a column vector $\mathbf{x}$ with the five astrometric parameters of a simulated or real star, such that $\boldsymbol{\Delta}\eta_5 = \mathbf{M} \cdot \mathbf{x}$ (Equation (3.4)), i.e.,

$$\begin{pmatrix} \Delta\eta_{5,1} \\ \Delta\eta_{5,2} \\ \vdots \\ \Delta\eta_{5,n} \end{pmatrix} = \begin{pmatrix} \sin\theta_1 & \cos\theta_1 & \Pi_{\eta,1} & \Delta t_1 \sin\theta_1 & \Delta t_1 \cos\theta_1 \\ \sin\theta_2 & \cos\theta_2 & \Pi_{\eta,2} & \Delta t_2 \sin\theta_2 & \Delta t_2 \cos\theta_2 \\ \vdots & \vdots & \vdots & \vdots & \vdots \\ \sin\theta_n & \cos\theta_n & \Pi_{\eta,n} & \Delta t_n \sin\theta_n & \Delta t_n \cos\theta_n \end{pmatrix} \begin{pmatrix} \Delta\alpha_* \\ \Delta\delta \\ \varpi \\ \mu_{\alpha*} \\ \mu_\delta \end{pmatrix}. \tag{3.9}$$

However, for the present purposes of estimating the detectability (see Section 2.4), the star parameters can all be set to 0, such that $\boldsymbol{\Delta}\eta_5 = \mathbf{0}$. This is possible because the system of equations is linear, so that the residuals of the least-squares fit does not depend on the actual values of the parameters.

Step 3. Keplerian displacement

To calculate the displacement due to the planet (Equation (3.5)), the Thiele-Innes constants A, B, F, G (Equation (2.8)) are calculated and put in a column vector $\mathbf{y}$ and the

---

[3] This approximate position of the star is computed in order to determine the number of field of view crossings. A more accurate determination of the position is possible, but is not likely to have a large effect on the results.

rest of the Keplerian parameters in a matrix $\mathbf{K}$, such that $\boldsymbol{\Delta}\eta_7 = \mathbf{K}\cdot\mathbf{y}$, i.e.,

$$\begin{pmatrix}\Delta\eta_{7,1}\\ \Delta\eta_{7,2}\\ \vdots\\ \Delta\eta_{7,n}\end{pmatrix} = \begin{pmatrix}\sin\theta_1 X_1 & \sin\theta_1 Y_1 & \cos\theta_1 X_1 & \cos\theta_1 Y_1\\ \sin\theta_2 X_2 & \sin\theta_2 Y_2 & \cos\theta_2 X_2 & \cos\theta_2 Y_2\\ \vdots & \vdots & \vdots & \vdots\\ \sin\theta_n X_n & \sin\theta_n Y_n & \cos\theta_n X_n & \cos\theta_n Y_n\end{pmatrix}\begin{pmatrix}B\\ G\\ A\\ F\end{pmatrix}, \tag{3.10}$$

where the eccentric anomaly $E(t_i)$ of the planet in X_i and Y_i (Equation (2.10)) have been calculated iteratively by solving Equation (2.7) with Newton's method (see, e.g., Montenbruck et al. (2002)).

Step 4. Making the final observation

The total displacement of the star and planet is the superposition of the astrometric and Keplerian displacements, i.e., the sum of Equations (3.9) and (3.10). To produce the final observation, $\boldsymbol{\Delta}\eta^{\text{obs}}$, a column vector ν with n elements containing normally distributed noise with standard deviation σ_i (Equation (2.12)) is added to the sum:

$$\begin{pmatrix}\Delta\eta_1^{\text{obs}}\\ \Delta\eta_2^{\text{obs}}\\ \vdots\\ \Delta\eta_n^{\text{obs}}\end{pmatrix} = \begin{pmatrix}\Delta\eta_{5,1}\\ \Delta\eta_{5,2}\\ \vdots\\ \Delta\eta_{5,n}\end{pmatrix} + \begin{pmatrix}\Delta\eta_{7,1}\\ \Delta\eta_{7,2}\\ \vdots\\ \Delta\eta_{7,n}\end{pmatrix} + \begin{pmatrix}\nu_1\\ \nu_2\\ \vdots\\ \nu_n\end{pmatrix}. \tag{3.11}$$

Note: To make the final observation for multiple-planet systems, Step 3 is repeated for every planet in the system and the resulting displacements are added to $\boldsymbol{\Delta}\eta^{\text{obs}}$.

Step 5. Joint fitting of the astrometric and Keplerian parameters

The fitting of the astrometric parameters requires a solution to the system of linear equations $\mathbf{M}\cdot\mathbf{z}_5 = \boldsymbol{\Delta}\eta^{\text{obs}}$ (where $\mathbf{z}_5$ corresponds to the vector $\mathbf{x}$ containing the astrometric parameters). Since $\mathbf{M}$ is not a square matrix, the resulting system of equations is overdetermined and lacks a unique solution. Thus, the fitting of the astrometric parameters requires a linear least squares method[4], i.e., finding the best-fit solution

$$\mathbf{z}_5 = \mathbf{M}^+ \cdot \boldsymbol{\Delta}\eta^{\text{obs}}, \tag{3.12}$$

where $\mathbf{M}^+$ is the pseudoinverse[5] of $\mathbf{M}$. The parameters in $\mathbf{z}_5$ are then used to produce the residuals of the observed and fitted astrometric displacement,

$$\mathbf{r}_5 = \boldsymbol{\Delta}\eta^{\text{obs}} - \mathbf{M}\cdot\mathbf{z}_5\,, \tag{3.13}$$

---

[4] In the commercial programming language and environment MATLAB, used in this thesis, there is a built-in linear least-squares solver which can be called with the backslash operator, e.g., `X = A\B` solves `A*X = B`, where `A` and `B` correspond to $\mathbf{M}$ and $\boldsymbol{\Delta}\eta^{\text{obs}}$, respectively, and `X` the solved-for vector $\mathbf{z}_5$.

[5] The generalized inverse of a matrix, applicable to rectangular matrices, as well as singular square matrices.

which is used to calculate the goodness-of-fit as measured by the chi-squared statistic

$$\chi_5^2 = \sum_i \left(\frac{\mathbf{r}_{5,i}}{\sigma_i} \right)^2 . \tag{3.14}$$

For the fitting of the Keplerian parameters, Ω, M_0 and i are simulated as before, but f_{true} is assumed to be unknown. For the purposes of this investigation, it is assumed that $e = 0$ in the fit, which simplifies the problem to a search for a minimum in the chi-squared statistic for a range of frequencies $0.01 \leq f \leq 500\ \text{yr}^{-1}$. The stepping size for the frequency is $\Delta f = 0.01$. For each searched frequency, a new $\mathbf{K}$ is calculated (see Step 3). With $e = 0$, ω becomes largely meaningless, Equation (2.7) reduces to $E = M_0$ and the solution for the remaining nine parameters becomes linear. The solution is obtained by creating a horizontally concatenated matrix with the $\mathbf{M}$ and $\mathbf{K}$ matrices: $\mathbf{Q} = (\mathbf{M}, \mathbf{K})$, and solving, as above, for a vector $\mathbf{z}_9 = \mathbf{Q}^+ \cdot \boldsymbol{\Delta\eta}^{\text{obs}}$, yielding the residuals $\mathbf{r}_9 = \boldsymbol{\Delta\eta}^{\text{obs}} - \mathbf{Q} \cdot \mathbf{z}_9$. The chi-squared statistic for the nine parameters, χ_9^2, is calculated as above, but for each of the searched frequencies.

Note: For multiple-planet systems, the orbit-fitting procedure is run n_{p} times. The first run is on the composite observation signal of all the planets, $\Delta\eta_1^{\text{obs}}$. The subsequent runs are on the residuals of the former observation signal after the former fitted observation has been subtracted, e.g., $\Delta\eta_2^{\text{obs}} = \Delta\eta_1^{\text{obs}} - \Delta\eta_1^{\text{fit}}$.

Step 6. Estimating the detectability

The detectability is estimated by calculating the $\Delta\chi^2$ metric (Equation (2.14))

$$\Delta\chi^2(f) = \chi_5^2 - \chi_9^2(f) \tag{3.15}$$

for every frequency f. The result is a periodogram as shown in Figure 3.3, in which the highest peak (in each diagram) corresponds to the minimum in χ_9^2 and best fitting frequency, f_{fit}. The S/N (Equation (2.13)) is estimated by computing α (Equation (2.2)) using the planet data and the magnitude (assuming $V = G$) of the host star (giving σ_{fov} according to Table 2.1).

Note: For multiple-planet systems, each planet has an associated $\Delta\chi^2$ calculated from the χ_9^2 of each planet.

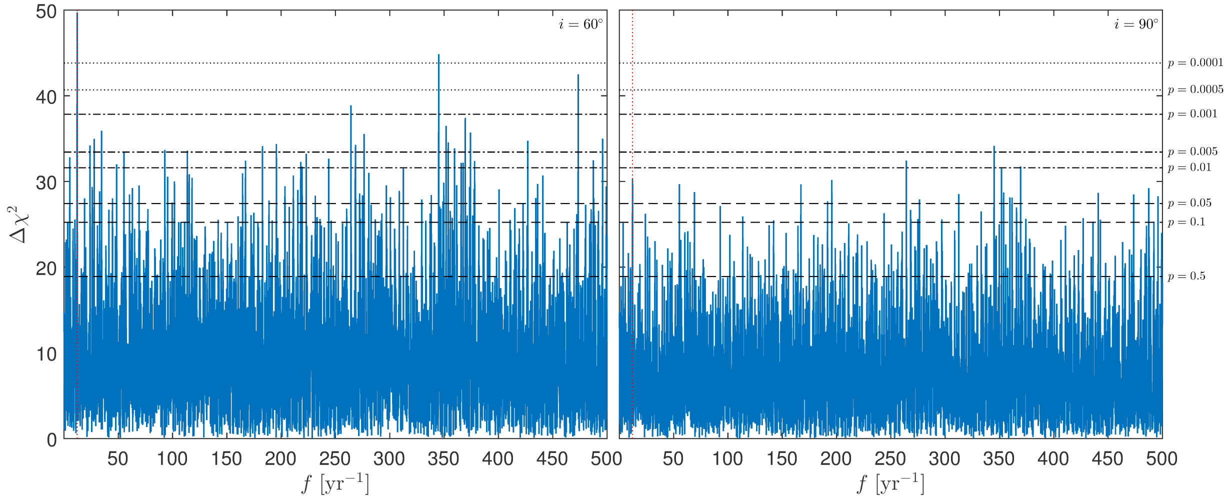

Figure 3.3: Example of two (individual orbit-fitting) $\Delta\chi^2(f)$-spectra for the planet GJ 876 c ($M_\mathrm{p}\sin i = 0.61\ \mathrm{M_J}$), assuming two different values of i, shown in the upper right corner (in both cases simulated $\Omega = 100^\circ$ and $M_0 = 0^\circ$). $f_\mathrm{true} = 12.14\ \mathrm{yr}^{-1}$ is marked by the red dotted vertical line in each diagram. The highest peak in the left diagram ($i = 60^\circ$) is at $\Delta\chi^2 = 49.7$ with $f_\mathrm{fit} = 12.18\ \mathrm{yr}^{-1}$. The highest peak in the right diagram ($i = 90^\circ$) is at $\Delta\chi^2 = 34.2$ with $f_\mathrm{fit} = 345\ \mathrm{yr}^{-1}$. The horizontal lines mark the significance levels of the peaks (see Section 3.1).

Step 7. Collecting the results

To quantify the detection of a planet, the *reliability* is defined as

$$R \equiv \frac{n_\mathrm{det}}{n_\mathrm{exp}} \tag{3.16}$$

where n_det is the number of times f_fit is determined within 0.05 yr^{-1} of f_true and n_exp the total number of experiments. Three levels of reliability are defined: secure detection ($R = 1$), marginal detection ($0.5 < R < 1$) unreliable or no detection ($R \leq 0.5$).

Chapter 4

Results

In this chapter, the statistics of the simulation experiments in the form of diagrams and a table are presented without comments. The discussion of the results is instead deferred to Chapter 5.

Figures 4.1 and 4.2 show the detectability metrics for the individual orbit-fitting investigation. Figures 4.3 and 4.4 show the performance with respect to the true eccentricity of the individual and composite orbit-fitting investigations, respectively.

Figure 4.5 shows how well the orbital periods could be determined in the individual and composite orbit-fitting in a side-by-side comparison, by showing the average of the fitted period against the true period. Figure 4.6 shows the same as Figure 4.5 but all the fitted periods instead of the average. Note that the symbols in Figures 4.5 and 4.6 now represent the value of $\Delta\chi^2$, as explained in the caption.

Table 4.1 shows the percentage of the planets of different reliability levels in both investigations. For the interested reader, the detailed results of the composite, multiple-planet orbit-fitting investigation are shown in Table A.1 in Appendix A.

Table 4.1: The percentage of planets found in the individual and composite orbit-fitting investigations, represented by the different levels of reliability, R. Each of the four inclinations, i, was run through 10 experiments.

	Individual				Composite				
i	10°	30°	60°	90°	10°	30°	60°	90°	Unit
$R = 1$	52	31	21	14	21	13	8	6	%
$0.5 < R < 1$	37	12	10	12	18	14	8	8	%
$R \leq 0.5$	11	57	69	74	61	73	84	86	%

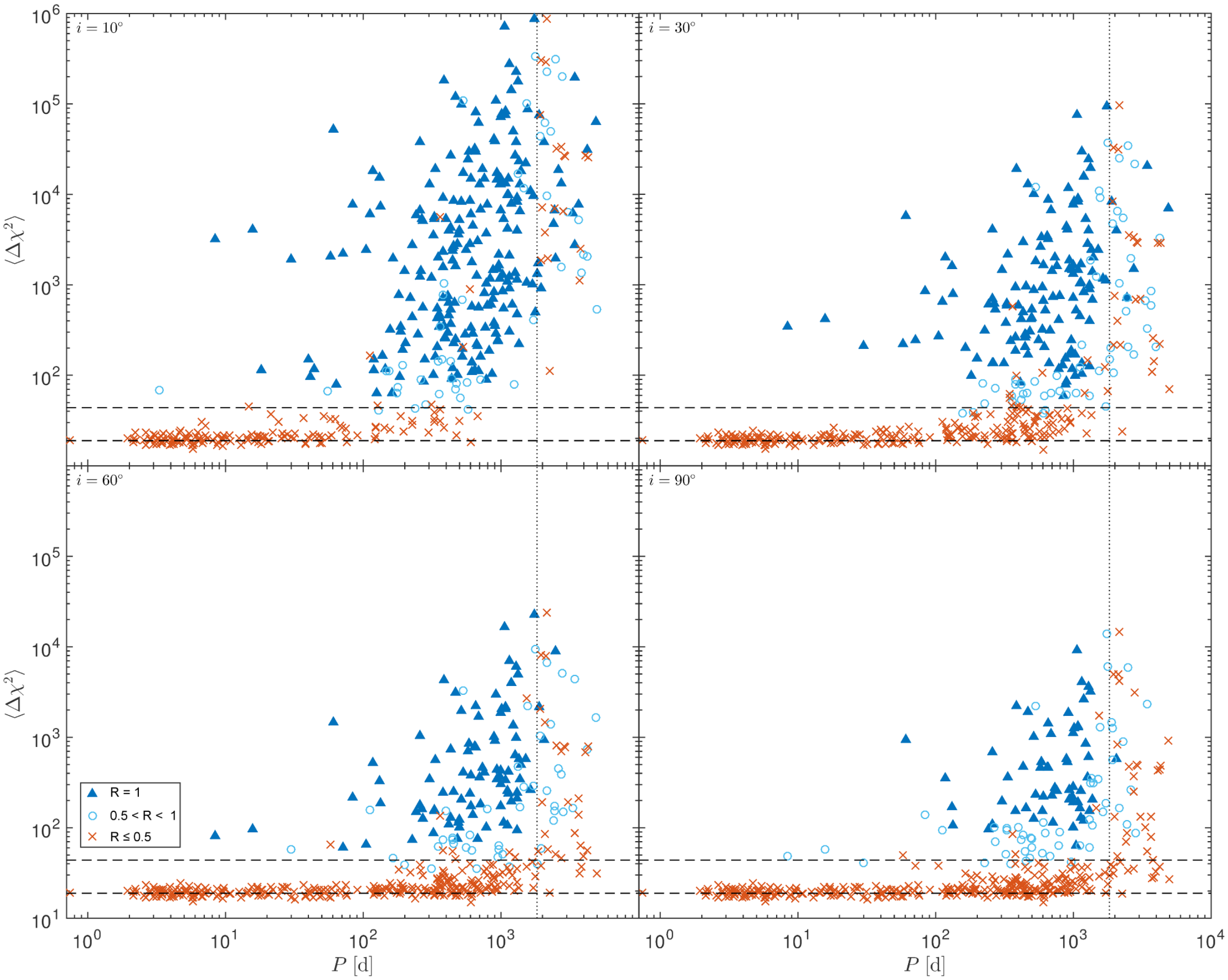

Figure 4.1: Results from the individual orbit-fitting investigation. The diagrams show the arithmetic mean of the $\Delta\chi^2$ detectability metric over the 10 experiments versus (true) orbital period. The upper and lower horizontal dashed lines indicate the empirical $\Delta\chi^2$-values 43.8 and 18.9, respectively, corresponding to the p-values 0.0001 and 0.5, respectively (see Figure 3.1). The vertical dotted line marks the mission lifetime of Gaia (5 years).

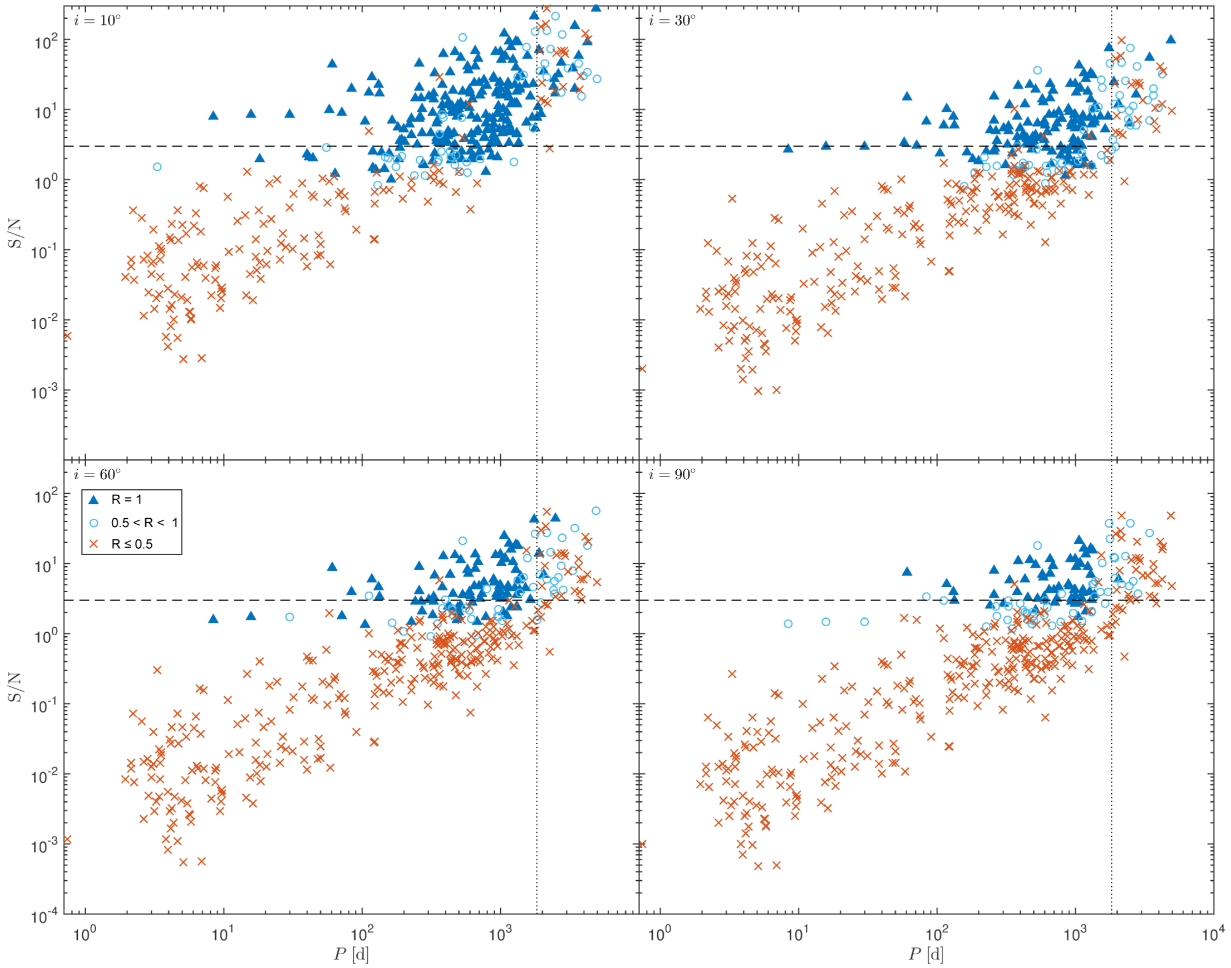

Figure 4.2: Results from the individual orbit-fitting investigation. The diagrams show the S/N versus orbital (true) period. The symbols represent planets with different reliability R (Equation (3.16)). The horizontal dashed line shows the S/N = 3 threshold. The vertical dotted line marks the mission lifetime of Gaia (5 years).

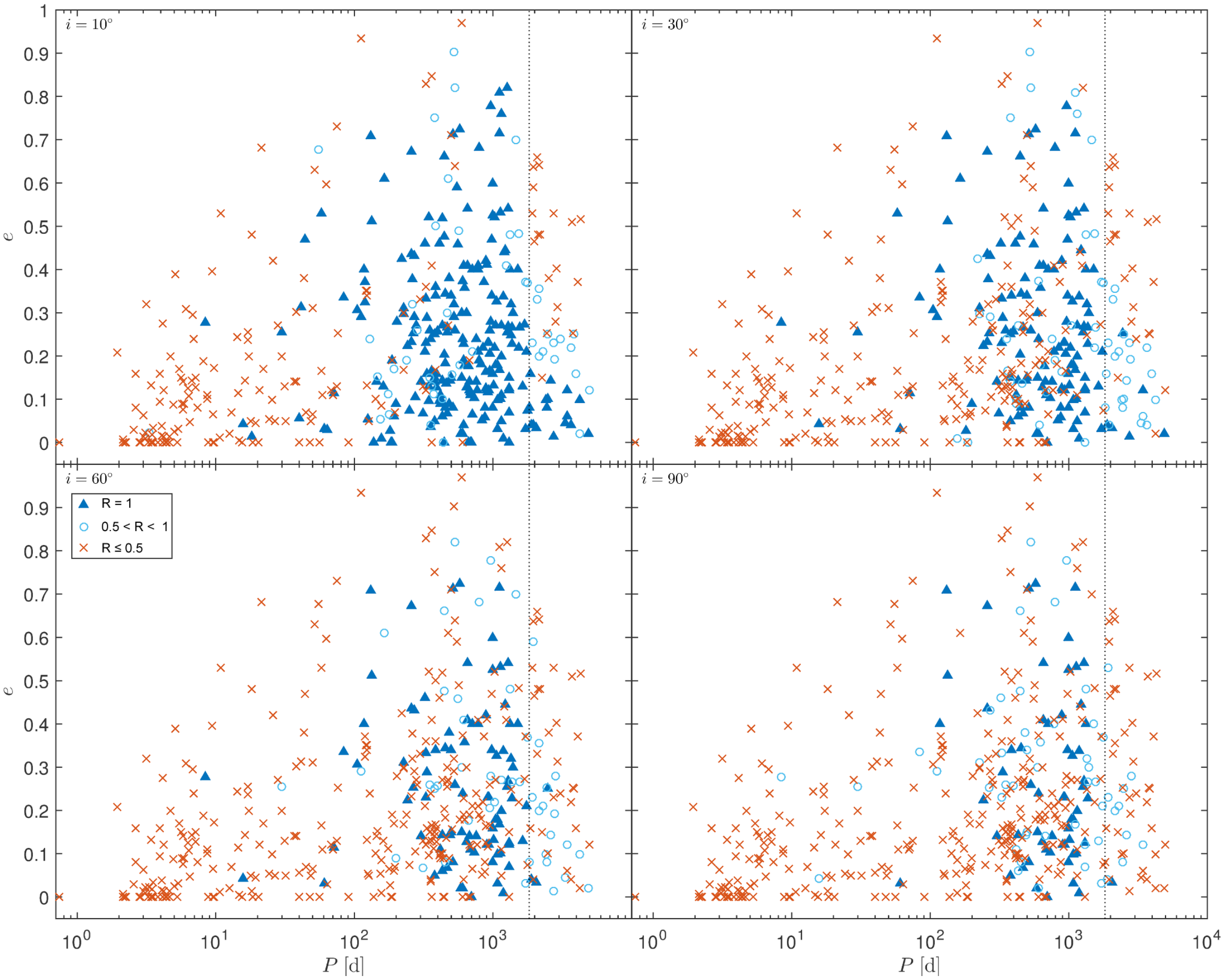

Figure 4.3: Results from the individual orbit-fitting investigation. The diagrams show the (true) eccentricity versus (true) orbital period. The symbols represent planets with different reliability R (Equation (3.16)). The vertical dotted line marks the mission lifetime of Gaia (5 years).

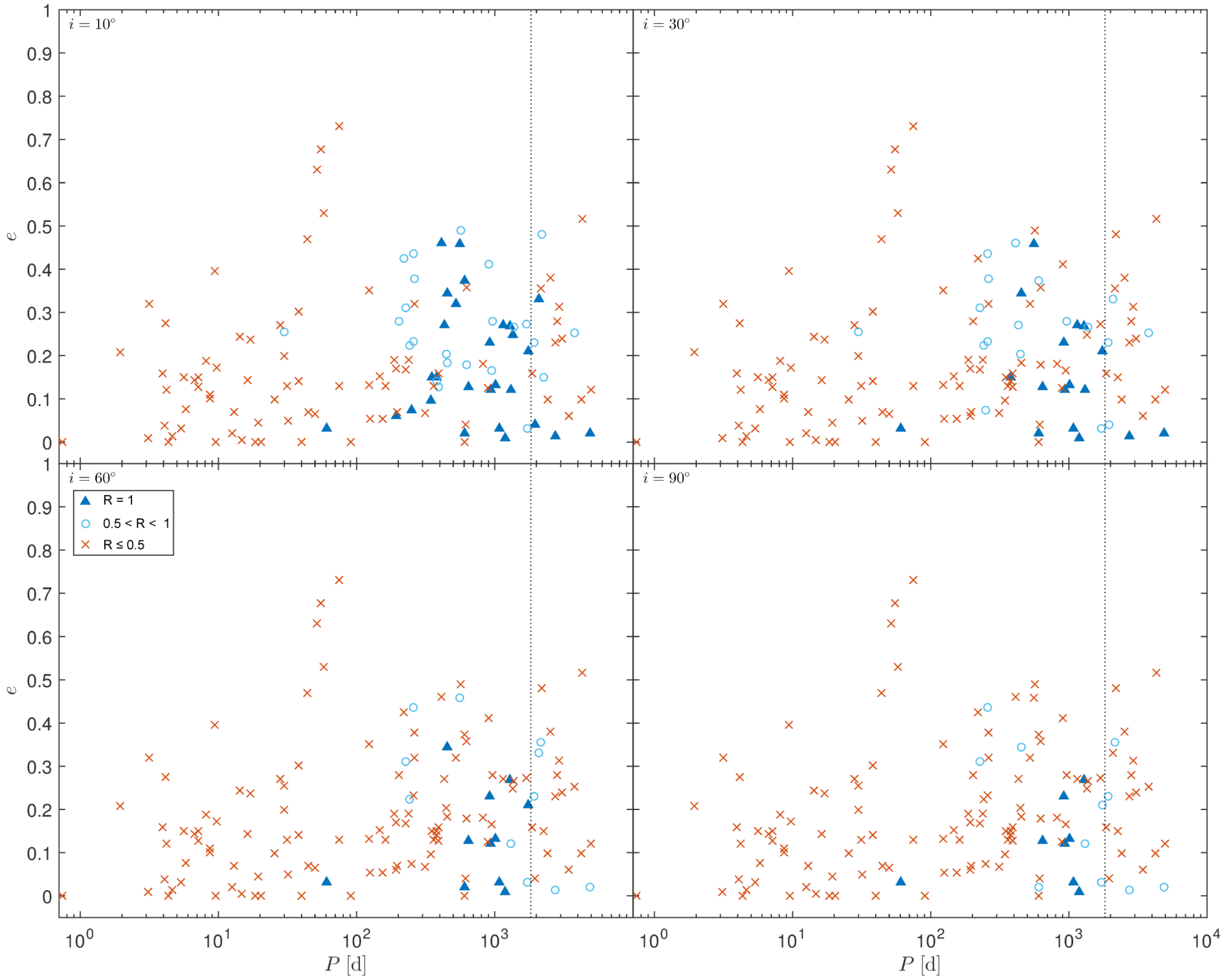

Figure 4.4: Results from the composite orbit-fitting investigation. The diagrams show the (true) eccentricity versus (true) orbital period. The symbols represent planets with different reliability R (Equation (3.16)). The vertical dotted line marks the mission lifetime of Gaia (5 years).

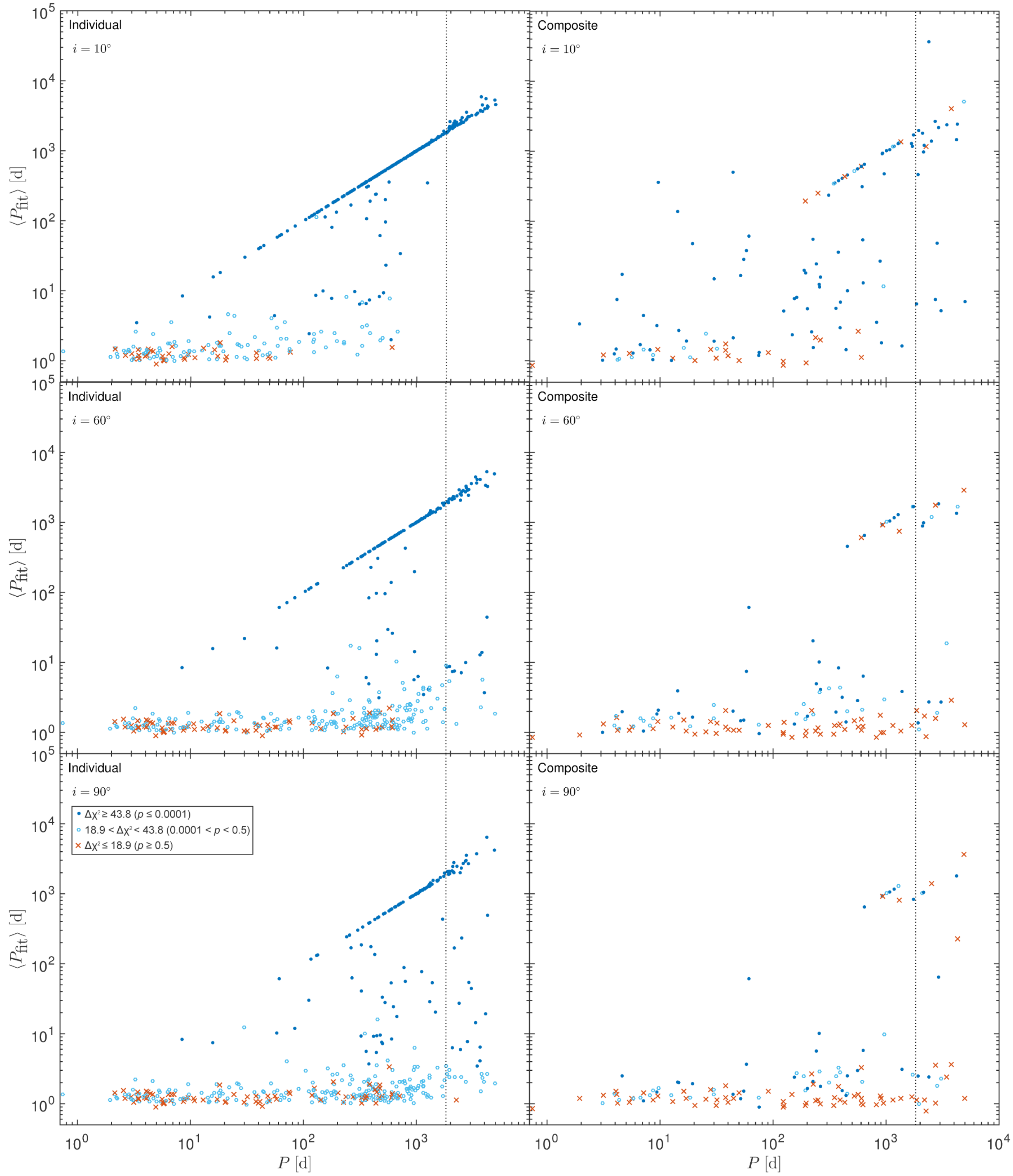

Figure 4.5: Results from the individual (left) and composite (right) orbit-fitting investigations. The diagrams show the arithmetic mean of the fitted period ($P_\mathrm{fit} = 1/f_\mathrm{fit}$) for 10 experiments versus the (true) orbital period. The vertical dotted line marks the mission lifetime of Gaia (5 years).

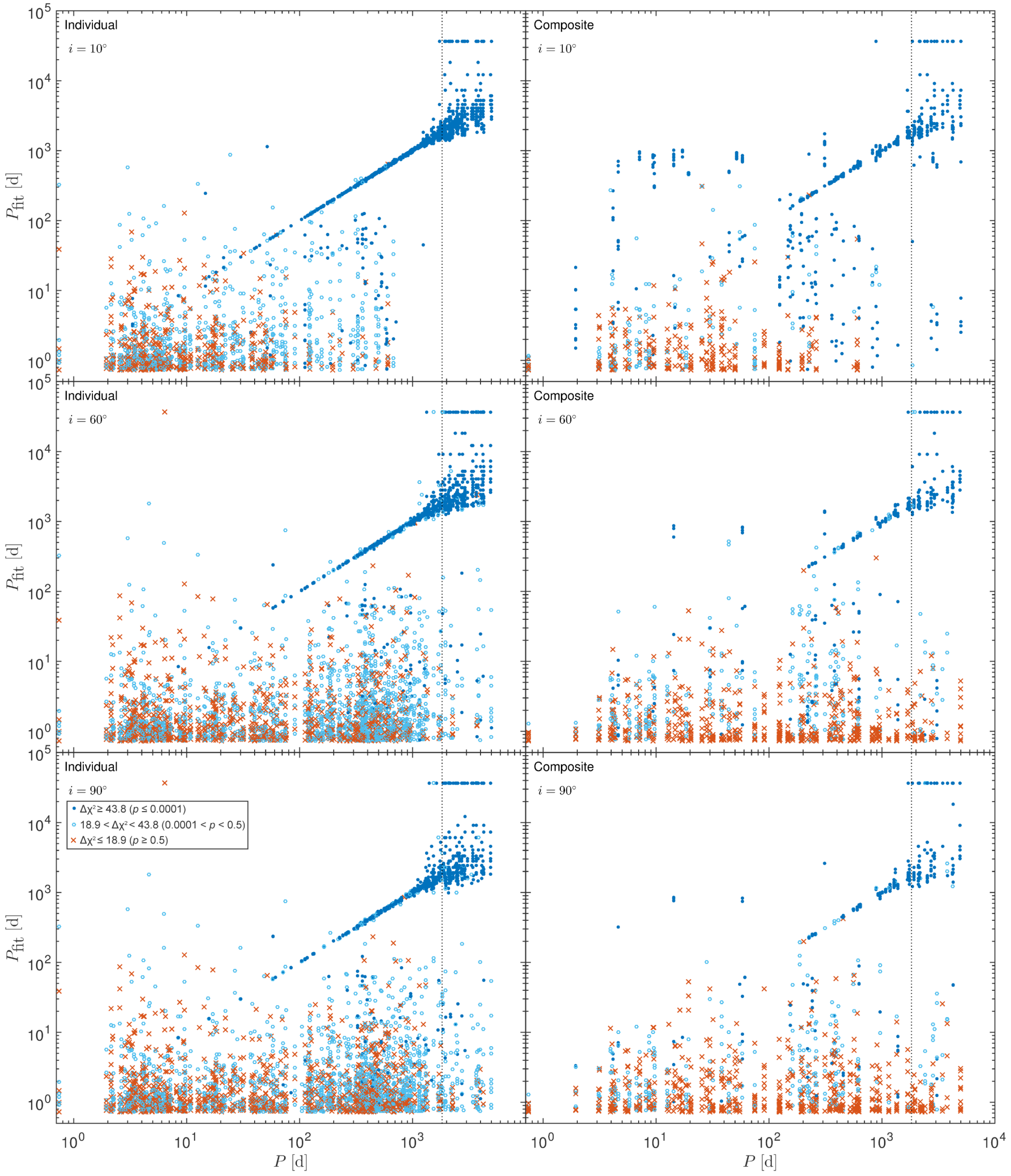

Figure 4.6: Results from the individual (left) and composite (right) orbit-fitting. Similarly to Figure 4.5, the diagrams show the fitted periods for 10 experiments versus the (true) orbital period. However, instead of the average, all the fitted periods are shown. Thus, every planet appears 10 times in each diagram, where the spread in P_{fit} appears in a column-like fashion. The vertical dotted line marks the mission lifetime of Gaia (5 years).

Chapter 5

Discussion and conclusions

It is evident that there is a significant difference in the overall detectability of the RV planets in the four assumed values of i, which necessitates a discussion of their respective applicability. For example, looking at Figure 3.3, it can be seen that the correct period is found for $i = 60°$ but not $90°$. Figure 5.1 shows a representative part of the mass distribution in the RV planet sample. As seen, the variability in mass is quite large between the smallest and largest values of i used in the investigations, with a less pronounced variability between the three larger angles, which explains the large difference between $i = 10°$ and $90°$, and the smaller difference between $i = 60°$ and $90°$, common to all the results. From geometric arguments it can be shown, assuming random inclinations, that the median inclination for exoplanet systems should be $i = 60°$. Therefore, the most optimistic and less realistic cases are assumed to be $i = 10°$ and $30°$. The results from these two inclinations can still be useful in measuring the performance of the algorithm and the detectability metrics, but probably says little about reality. With the geometric argument in mind and disregarding the selection effects of the RV method, which favors larger inclinations, the most realistic case is assumed to be $i = 60°$, and $i = 90°$ is seen as the most restrictive, worst-case scenario.

In general, all diagrams in Figures 4.1–4.4 restrict most of the secure detections to periods between about 0.2 and 6 years, confirming the conclusion of Perryman et al. (2014) that this is the period range where Gaia is most efficient at detecting exoplanets. The results from this investigation thus indicate that, taking the $i = 60°$ as the most realistic case, Gaia will likely be able to detect and characterize around a third (with 21% secure and 10% marginal detections, see Table 4.1) of the planets in the current RV catalog, most of which with periods between 0.2 and 6 years. This could be taken as a lower bound, since a fit assuming a circular orbit is probable to have missed some planets, but must also be seen in the context of the 55 multiple-planet systems in the sample, with a total of 132 members (30% of the total sample). For the multiple-planet systems, the composite orbit-fitting yields only 16% detections with $i = 60°$ (with 8% secure and 8% marginal detections, see Table 4.1). This low number may reflect the fact that the majority of the multiple-planet system members have periods outside the most efficient range of Gaia, or be due to poor performance of the algorithm in the composite orbit-fitting.

There are a number of potential reasons for the reduction in performance in the composite orbit-fitting of the multiple-planet systems: a) in systems where the algorithm, for whatever reason, finds the wrong period, it simply removes the corresponding fitted stellar image displacement, which could overlap the displacements from the real signals or produce other significant peaks in $\Delta\chi^2$, thus reducing the detectability of any planet in the system; b) the introduction of several Keplerian signals increases the risk of significant peaks due to aliasing; c) the adding of several eccentric Keplerian signals may produce resonances that show up as significant peaks.

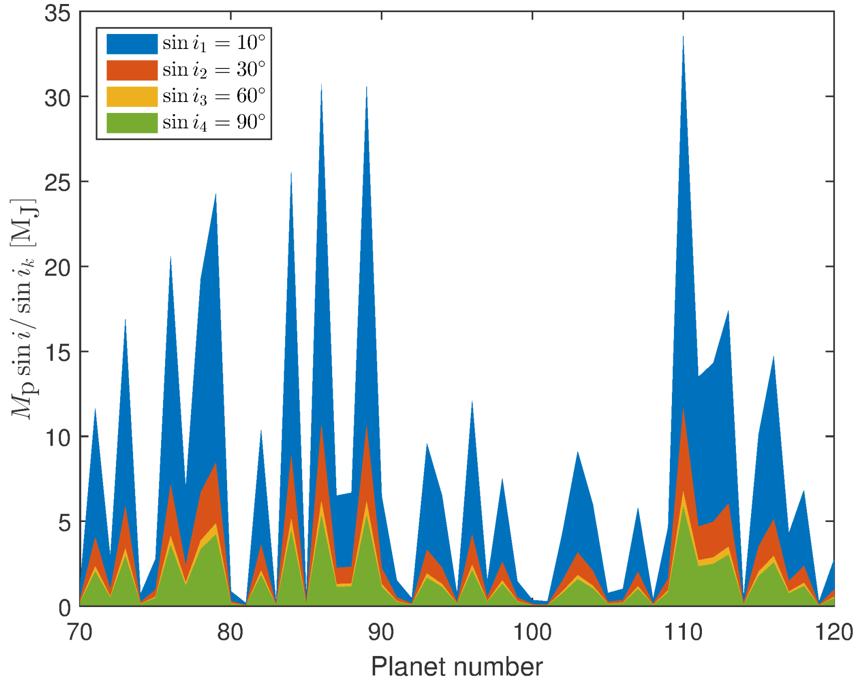

Figure 5.1: The discrete mass distribution of a representative part of the RV planet sample. The areas under the curves are colored to facilitate visibility.

In Figures 4.5 and 4.6 the filled blue circles on average follow a diagonal line, which implies that the $\Delta\chi^2 > 43.8$ ($p < 0.0001$) mostly ensures a correct period estimation. The spread of the many blue filled circles in the longer periods (the upper right corners of the diagrams) also indicate that the quality of the fits degrade as the periods become larger than the mission lifetime. (It is worth pointing out that the log-scale makes the spread of the points in the lower part of the diagram look larger than in the upper part, but in reality it is the other way around.) It is interesting to note that in the spread of the filled blue circles, many lie along the same horizontal line. These lines are probably due to the step-size in f in the $\Delta\chi^2(f)$-spectrum being too large for the peaks to be distinguishable at the lowest frequencies, and many of the found frequencies are at the lowest frequency (0.01 yr^{-1}). Another interesting feature is that the average of the fitted periods over the 10 experiments (Figure 4.5) for true periods larger than five years tend to the diagonal line and thus the true period. Another suspected case of aliasing (or the other effects due to the composite signal, see above) can be seen in the right-hand side diagrams in the figures, where many filled blue circles do not follow the diagonal line. The orbits found in these cases are, by their large $\Delta\chi^2$, clearly highly significant, but also clearly wrong.

Perhaps the most striking overall result is that the assumption of a circular orbit in the fit still yields the correct orbital period for a sizable fraction of the detectable planets. It is evident from Figure 4.3 that there is a large spread in e of secure and marginal detections across all four inclinations. A tantalizing conclusion is that a detection with this algorithm is largely independent of the actual eccentricity of the planet. It seems that the periods of most of the planets with eccentricity below 0.8 can be reliably determined. The same positive result is not as evident in the composite multiple-planet fits, as seen in Figure 4.4, where a smaller number of planets are correctly determined, especially for inclinations 60° and 90°. In the composite case, the upper threshold seems to be $e \simeq 0.5$. However, there are evidently no multiple-planet system members with $e > 0.5$ in the period range where Gaia is most efficient, which might be what is limiting the threshold. Arguably, there is an overall lack of planets in the higher eccentricities in the RV sample to definitively set a threshold in either case. Therefore, further similar investigations with synthetic planets and a flatter distribution of eccentricities is proposed.

It is found that the orbit-fitting algorithm performed largely in agreement with past estimates of the two detectability metrics $\Delta\chi^2$ and the S/N. The majority of the overall detections (blue triangles and circles) in Figure 4.1, for all four inclinations, consistently reside above $\Delta\chi^2 = 43.8$ ($p = 0.0001$), with almost none below. However, the secure detections start being in the majority only above $\Delta\chi^2 \simeq 100$. Thus, it seems reasonable to require $\Delta\chi^2 > 100$ to ensure secure detections. This requirement is in line with Perryman et al. (2014), who considered a $\Delta\chi^2 \simeq 30$ as providing marginal detections and saw that a $\Delta\chi^2 > 100$ yielded solutions with orbital parameters determined to 10% or better, which is here taken to be roughly equivalent to a secure detection ($R = 1$). Concerning the S/N, it can be inferred from Figure 4.2 that the threshold of S/N = 3 is quite restrictive for all inclinations. In $i = 10°$, there are a large number of secure and marginal detections above even S/N = 1. For the remaining three inclinations, a majority of detections reside above S/N = 2. A detection threshold of S/N = 2 could therefore be used without risking too many false detections, likewise in accordance with Perryman et al. (2014).

If the algorithm is employed on, e.g., 10^7 stars in the Gaia data, the number of false alarms with $\Delta\chi^2 \geqslant 43.8$ ($p \leqslant 0.0001$) is 10^3. The same number for planets with $\Delta\chi^2 \geqslant 100$ is not quantified here, but a reasonable guess is that it is at least one order of magnitude smaller. Moreover, since the false alarm probability increases with the searched frequency range, ways to decrease this range is desirable. E.g., an upper limit at a period near the Gaia mission lifetime can be set, or the algorithm can be made to check for stars where high frequencies can be ruled out, due to e.g. engulfment, and decrease the range accordingly.

There is an effect from the parallax seen as either a sharp peak or dip at $f = 1$ yr^{-1} in the $\Delta\chi^2(f)$-spectrum, resulting from the orbital period of Gaia around the Sun. It was suspected that this would affect the detectability of planets with orbital periods close to one year. However, in a test with all four inclinations used in the investigation for a handful of planets with such a period (e.g., HD 96063 b, HD 38283 b and HD 212771 b with respective periods 361.1, 363.2, 373.3 d), there was either no evidence of any peak from the orbit-fitting at all, which could be attributed to a too small astrometric signature, or the peak was found to dominate the small parallax dip/peak. It is still recognized that the parallax could be a factor in cases with noise close to the single-measurement uncertainty, but considering the fact that no significant effect was found in the small inspection above and that not many RV planets have a period very close to one year, the overall impact of the parallax effect in this investigation is deemed to be negligible.

The potential for the combination of Gaia data with other types of measurements is substantial. The synergies between RV and astrometry is particularly notable. Both can determine the parameters $a_{\mathrm{p}}, e, \omega, M_0$ and P, which will consequently improve their constraints in a combined measurement. Importantly, astrometry provides i (for non-transiting planets), and thus enables the determination of the unique mass of the planet. Furthermore, information on which of the nodes is ascending can be supplied by RV, something astrometry alone cannot decide (Perryman et al., 2014). Another notable feature is that, by doing follow-up measurements of stars with long-period, high-mass planets identified by Gaia, high-precision RV can potentially detect planets with smaller semi-major axes that Gaia might have missed due to not being sensitive enough in that region (Sozzetti, 2015). In addition to high-precision follow-up of the potentially thousands transiting planets detected by Gaia photometry, there is expected to be on the order of 100 transiting planets with intermediate separation in the Gaia astrometric data (Perryman et al., 2014). The intermediate separation transiting planets constitute particularly interesting follow-up targets for a systematic comparison with the Hot Jupiters (Sozzetti, 2015). As for targets of direct optical imaging, Gaia will be able to identify the optimal visibility of a list of planets by providing the epoch and location of maximum brightness (Sozzetti, 2015).

Looking to the future, after the full release of its data[1], Gaia will likely have provided many new insights into the properties of many of the known planets, supplied a large amount of new giant planet detections, generated rich statistics and informed planetary formation and evolution theories, as well as yielded many opportunities for synergies with other techniques. Beyond Gaia, the tantalizing advent of sub-µas astrometry will enable the detection of terrestrial planets around nearby stars. However, since the ambitious Space Interferometry Mission (SIM) by the U.S. National Aeronautics and Space Administration (NASA) was discontinued, there are few concrete plans for space-based astrometric observatories. One glimmer of hope is that the Chinese Strategic Pioneer Program (SPP)

---

[1] The first orbital solutions are expected earliest in 2017. The full catalog is scheduled for release in 2022. For up-to-date information, see `http://www.cosmos.esa.int/web/gaia/release`.

on Space Science approved in 2013 the Search for Terrestrial ExoPlanets (STEP) mission with a purported ∼0.5–1 µas accuracy, thus capable of detecting Earth-mass planets around solar-type stars out to 20 pc (Chen, 2014). However, no launch date is set and not much information about STEP is available. The prospects for ground-based sub-µas astrometry remain limited by the practical limits imposed by atmospheric noise (Sozzetti, 2010). Possible technological workarounds utilizing adaptive optics and interferometry are being developed, but overcoming atmospheric noise remains a great challenge (see, e.g., Sozzetti (2010)).

In conclusion, an orbit-fitting algorithm assuming a circular orbit in the fit can correctly and reliably determine the orbital period for planets with eccentricity $\lesssim 0.8$ in single-planet systems, and $\lesssim 0.5$ in multiple-planet systems. Further investigations with synthetic planets are called for to set more stringent limits on the eccentricity and further evaluate the overall feasibility of this approach. The small investigation conducted in this thesis tentatively indicates that this approach, which significantly reduces computational load, can potentially be used to expand the number of stars that can be searched for planets in the Gaia data. Further, this investigation has found that around one third of the total number of planets in the current RV catalog, and one sixth of the multiple-planet system members, can reliably or somewhat reliably be detected and characterized by Gaia.

Acknowledgments

I would like to extend my acknowledgment and sincerest thanks to my supervisor, Lennart Lindegren, who came up with the idea for this project and showed both interest and enthusiasm for my progress, as well as provided help, input and guidance when needed and in the right amounts. Thank you, Lennart.

Bibliography

Binnendijk, L. 1960, Properties of Double Stars; A Survey of Parallaxes and Orbits. (University of Pennsylvania Press)

Casertano, S., Lattanzi, M. G., Sozzetti, A., et al. 2008, A&A, 482, 699

Chen, D. 2014, Journal of Instrumentation, 9, C4040

de Bruijne, J. H. J. 2012, ApSS, 341, 31

Holl, B., Lindegren, L., & Hobbs, D. 2012, A&A, 543, A15

Holmberg, E. 1938, Invisible Companions of Parallax Stars Revealed by Means of Modern Trigonometric Parallax Observations, Meddelanden från Lunds astronomiska observatorium: Ser. 2 (Observatoriet)

Ida, S., & Lin, D. N. C. 2008, ApJ, 673, 487

Kaplan, G. H. 2005, U.S. Naval Observatory Circulars, 179

Livio, M., Sahu, K., & Valenti, J. 2011, A Decade of Extrasolar Planets around Normal Stars

Mayor, M., & Queloz, D. 1995, Nature, 378, 355

Montenbruck, O., Pfleger, T., & Dunlop, S. 2002, Astronomy on the Personal Computer (Springer)

Muterspaugh, M. W., Lane, B. F., Kulkarni, S. R., et al. 2010, AJ, 140, 1657

Perryman, M. 2011, The Exoplanet Handbook (Cambridge University Press)

Perryman, M., Hartman, J., Bakos, G. Á., & Lindegren, L. 2014, ApJ, 797, 14

Press, W. H., Teukolsky, S. A., Vetterling, W. T., & Flannery, B. P. 2007, Numerical Recipes 3rd Edition: The art of Scientific Computing (Cambridge University Press)

Seidelmann, P. K. 1992, Explanatory Supplement to the Astronomical Almanac. A revision to the Explanatory Supplement to the Astronomical Ephemeris and the American Ephemeris and Nautical Almanac. (P. K.. University Science Books)

Sozzetti, A. 2010, in EAS Publications Series, Vol. 42, EAS Publications Series, ed. K. Goździewski, A. Niedzielski, & J. Schneider, 55–77

Sozzetti, A. 2011, in EAS Publications Series, Vol. 45, EAS Publications Series, 273–278

Sozzetti, A. 2015, ArXiv e-prints, arXiv:1502.03575

van de Kamp, P. 1963, AJ, 68, 515

Wright, J. T., & Howard, A. W. 2009, ApJS, 182, 205

Appendix A

Table of the multiple-planet composite fit results

Table A.1 shows the results of the multiple-planet composite fits.

Table A.1: Detailed results of the composite orbit-fitting investigation. All 55 multiple-planet systems are subjected to four sets of 10 experiments, each set with a different assumed inclination, i. For each set, the average f_{fit} (determined within 0.05 yr^{-1} of f_{true}), and the average $\Delta\chi^2$ are shown. The reliability, R, is shown with zeros redacted to facilitate oversight. All system host stars have $V \leq 12$ and thus $\sigma_{\mathrm{fov}} = 34.2$ µas. The minimum mass of the planet, $M_{\mathrm{p}} \sin i$, is given in M_{J} and the astrometric signature, α, in µas.

				$i = 10°$				$i = 30°$				$i = 60°$				$i = 90°$			
Planet	$M_p \sin i$	e	f_{true}	α	$\langle\Delta\chi^2\rangle$	R	$\langle f_{\mathrm{fit}}\rangle$	α	$\langle\Delta\chi^2\rangle$	R	$\langle f_{\mathrm{fit}}\rangle$	α	$\langle\Delta\chi^2\rangle$	R	$\langle f_{\mathrm{fit}}\rangle$	α	$\langle\Delta\chi^2\rangle$	R	$\langle f_{\mathrm{fit}}\rangle$
24 Sex b	1.84	0.18	0.80	101.6	138	.6	0.80	35.3	51	.1	0.79	20.4	26		184.17	17.6	24		262.31
24 Sex c	1.52	0.41	0.40	133.3	361	.7	0.40	46.3	23		399.88	26.7	14		368.03	23.1	14		302.89
47 UMa b	2.55	0.03	0.34	1967.9	79478	1.0	0.35	683.4	8610	1.0	0.35	394.6	2138	1.0	0.35	341.7	1342	1.0	0.35
47 UMa c	0.55	0.10	0.15	717.1	1692		0.01	249.0	179		12.77	143.8	53		133.85	124.5	45		151.37
55 Cnc b	0.80	0.00	24.93	44.7	26		133.11	15.5	11		116.08	9.0	9		194.38	7.8	8		181.67
55 Cnc c	0.16	0.07	8.23	19.2	7		169.45	6.7	6		318.99	3.9	5		340.48	3.3	5		309.10
55 Cnc d	3.54	0.02	0.07	9553.2	60712	1.0	0.07	3317.8	6691	1.0	0.07	1915.5	1780	.6	0.09	1658.9	1178	.7	0.09
55 Cnc e	0.03	0.00	495.90	0.2	12		420.76	0.1	22		395.25	0.0	17		424.42	0.0	17		431.36
55 Cnc f	0.17	0.32	1.40	65.8	84	.1	1.40	22.9	3		397.57	13.2	3		382.51	11.4	3		370.61
61 Vir b	0.02	0.12	86.65	0.5	22		352.48	0.2	18		339.66	0.1	17		339.66	0.1	17		357.59
61 Vir c	0.03	0.14	9.61	4.9	9		257.73	1.7	7		277.98	1.0	7		305.95	0.9	7		297.30
61 Vir d	0.07	0.35	2.97	23.2	5		416.58	8.1	4		405.85	4.6	4		385.65	4.0	4		406.45
BD -08 2823 b	0.05	0.15	65.22	0.4	36		324.67	0.2	18		221.53	0.1	16		306.97	0.1	16		307.17
BD -08 2823 c	0.33	0.19	1.54	39.0	11	.5	1.54	13.5	8		336.22	7.8	8		344.55	6.8	8		330.22
BD +20 2457 b	11.89	0.15	0.96	323.7	1383	1.0	0.96	112.4	154	1.0	0.97	64.9	47	.1	0.98	56.2	37	.2	0.97
BD +20 2457 c	6.90	0.18	0.59	122.8	198	.9	0.59	42.7	31	.2	0.59	24.6	15		297.86	21.3	13		374.25
GJ 163 b	0.03	0.11	42.32	1.9	22		347.31	0.7	18		326.04	0.4	23		232.04	0.3	21		233.38
GJ 163 c	0.02	0.10	14.25	2.5	15		149.27	0.9	13		320.00	0.5	14		354.60	0.4	14		312.60
GJ 163 d	0.09	0.37	0.60	87.5	306	1.0	0.61	30.4	39	.9	0.61	17.5	11		237.79	15.2	10		309.73
GJ 581 b	0.05	0.03	68.03	5.8	11		281.67	2.0	10		335.36	1.2	11		335.36	1.0	11		344.20
GJ 581 c	0.02	0.07	28.27	3.5	6		331.91	1.2	6		308.98	0.7	6		303.07	0.6	6		336.93
GJ 581 e	0.01	0.32	115.97	0.5	19		298.73	0.2	19		278.69	0.1	19		278.69	0.1	19		278.69
GJ 667 C b	0.02	0.15	50.73	2.0	20		251.42	0.7	19		249.39	0.4	19		251.11	0.4	19		254.49
GJ 667 C c	0.01	0.27	13.00	3.8	14		249.89	1.3	14		269.25	0.8	14		253.32	0.7	14		230.35
GJ 876 b	1.95	0.03	5.98	1484.7	47216	1.0	5.98	515.6	5091	1.0	5.98	297.7	1247	1.0	5.98	257.8	809	1.0	5.98
GJ 876 c	0.61	0.26	12.14	290.7	1356	.9	12.14	101.0	146	.9	12.14	58.3	15	.2	12.12	50.5	13	.2	12.13
GJ 876 d	0.02	0.21	188.49	1.4	176		107.29	0.5	28		292.96	0.3	39		399.15	0.2	28		304.57
GJ 876 e	0.04	0.06	2.94	47.9	68		70.18	16.6	14		171.83	9.6	9		262.28	8.3	8		388.45
HD 10180 c	0.04	0.08	63.42	0.4	21		280.30	0.1	25		319.41	0.1	22		300.09	0.1	22		303.64
HD 10180 d	0.04	0.14	22.33	0.6	12		237.37	0.2	15		244.14	0.1	13		240.09	0.1	13		244.70
HD 10180 e	0.08	0.07	7.34	2.9	8		359.23	1.0	9		277.37	0.6	8		340.86	0.5	8		257.84
HD 10180 f	0.07	0.13	2.98	4.9	5		368.25	1.7	5		273.21	1.0	5		366.27	0.8	5		343.63
HD 10180 g	0.07	0.00	0.61	12.7	3		318.52	4.4	4		387.07	2.6	4		337.86	2.2	3		360.61
HD 10180 h	0.21	0.15	0.16	93.8	106	.7	0.17	32.6	3		383.50	18.8	3		415.80	16.3	3		464.07
HD 108874 b	1.29	0.13	0.93	123.5	168	.6	0.93	42.9	26	.1	0.88	24.8	43		83.10	21.4	33		131.45
HD 108874 c	1.03	0.27	0.22	258.6	1168	.8	0.21	89.8	136	.5	0.22	51.8	14	.1	0.24	44.9	11	.1	0.24
HD 11964 b	0.61	0.04	0.19	294.9	867	1.0	0.19	102.4	92	.7	0.19	59.1	11		331.24	51.2	9		368.65
HD 11964 c	0.08	0.30	9.63	2.7	13		207.81	0.9	13		170.34	0.5	31		176.60	0.5	25		200.66
HD 125612 b	3.07	0.46	0.65	388.4	2040	1.0	0.65	134.9	223	1.0	0.65	77.9	61	.7	0.65	67.5	44	.5	0.64
HD 125612 c	0.06	0.27	87.91	0.3	55		48.11	0.1	16		209.59	0.1	13		222.67	0.0	12		266.24
HD 12661 b	2.34	0.38	1.39	271.7	891	.7	1.40	94.4	103	.6	1.39	54.5	32		89.04	47.2	25		205.76
HD 12661 c	1.95	0.03	0.21	787.8	12229	.9	0.21	273.6	1333	.9	0.21	158.0	337	.9	0.21	136.8	207	.7	0.21

				$i = 10^\circ$				$i = 30^\circ$				$i = 60^\circ$				$i = 90^\circ$			
Planet	$M_p \sin i$	e	$f_{\rm true}$	α	$\langle \Delta\chi^2 \rangle$	R	$\langle f_{\rm fit} \rangle$	α	$\langle \Delta\chi^2 \rangle$	R	$\langle f_{\rm fit} \rangle$	α	$\langle \Delta\chi^2 \rangle$	R	$\langle f_{\rm fit} \rangle$	α	$\langle \Delta\chi^2 \rangle$	R	$\langle f_{\rm fit} \rangle$
HD 128311 b	1.46	0.35	0.80	637.1	7714	1.0	0.80	221.3	819	1.0	0.80	127.8	185	1.0	0.80	110.6	108	.8	0.80
HD 128311 c	3.25	0.23	0.40	2281.6	115096	1.0	0.40	792.4	12208	1.0	0.40	457.5	2827	1.0	0.39	396.2	1677	1.0	0.39
HD 134987 b	1.56	0.23	1.41	251.5	1221	.7	1.42	87.3	139	.6	1.42	50.4	43	.2	1.43	43.7	32	.2	1.43
HD 134987 c	0.80	0.12	0.07	933.4	264	.2	0.09	324.2	29		129.87	187.2	14		283.03	162.1	11		304.67
HD 13908 b	0.87	0.05	18.84	8.0	56		7.64	2.8	20		232.17	1.6	18		220.89	1.4	18		188.67
HD 13908 c	5.13	0.12	0.39	624.6	17706	1.0	0.39	216.9	1879	1.0	0.39	125.2	434	1.0	0.40	108.5	253	1.0	0.40
HD 147018 b	2.13	0.47	8.26	70.2	377		0.73	24.4	47		83.15	14.1	24		181.04	12.2	21		266.82
HD 147018 c	6.59	0.13	0.36	1750.6	79993	1.0	0.36	608.0	8587	1.0	0.36	351.0	2035	1.0	0.36	304.0	1189	1.0	0.36
HD 154857 b	2.25	0.46	0.89	144.6	615	1.0	0.89	50.2	68	.9	0.88	29.0	23	.2	0.87	25.1	19	.1	0.92
HD 154857 c	2.58	0.06	0.11	688.4	3153	.4	0.11	239.1	331	.3	0.09	138.0	75	.1	0.07	119.5	52	.1	0.08
HD 155358 b	0.82	0.17	1.88	73.6	62	.1	1.84	25.6	39		142.19	14.8	23		237.43	12.8	22		234.11
HD 155358 c	0.81	0.16	0.93	115.7	292	.5	0.93	40.2	18	.2	0.96	23.2	13		276.59	20.1	13		324.59
HD 159243 b	1.13	0.02	28.94	8.8	16		356.87	3.1	15		281.37	1.8	23		226.81	1.5	20		278.37
HD 159243 c	1.90	0.08	1.47	108.0	306	1.0	1.47	37.5	43	.6	1.46	21.7	13		312.39	18.8	12		320.69
HD 159868 b	2.20	0.01	0.31	407.9	8461	1.0	0.31	141.7	899	1.0	0.31	81.8	214	1.0	0.31	70.8	130	1.0	0.31
HD 159868 c	0.73	0.15	1.04	60.5	147	1.0	1.04	21.0	23	.2	1.02	12.1	18		290.21	10.5	18		296.86
HD 163607 b	0.77	0.73	4.85	20.2	24		274.12	7.0	17		364.35	4.0	17		379.00	3.5	16		408.16
HD 163607 c	2.29	0.12	0.28	405.2	3790	1.0	0.28	140.7	418	1.0	0.27	81.3	109	.8	0.28	70.4	71	.8	0.27
HD 168443 b	7.70	0.53	6.29	334.0	5470	.1	6.24	116.0	570	.1	6.24	67.0	121		48.99	58.0	59		99.57
HD 168443 c	17.39	0.21	0.21	7323.5	808725	1.0	0.21	2543.4	84753	1.0	0.22	1468.4	18697	1.0	0.22	1271.7	10778	.8	0.22
HD 169830 b	2.89	0.31	1.62	250.9	2265	.6	1.61	87.1	247	.6	1.61	50.3	65	.7	1.61	43.6	43	.7	1.61
HD 169830 c	4.06	0.33	0.17	1562.8	61737	1.0	0.20	542.8	6389	.9	0.20	313.4	1357	.6	0.18	271.4	739	.3	0.17
HD 181433 b	0.02	0.40	38.96	0.5	137		113.29	0.2	25		215.32	0.1	33		199.02	0.1	25		248.12
HD 181433 c	0.64	0.28	0.38	296.3	2661	.8	0.40	102.9	296	.8	0.40	59.4	83	.3	0.41	51.4	57	.3	0.39
HD 181433 d	0.54	0.48	0.17	426.3	1053	.6	0.18	148.1	125	.5	0.18	85.5	17		212.27	74.0	13	.1	0.19
HD 183263 b	3.57	0.36	0.58	474.2	2377	.3	0.58	164.7	258	.4	0.58	95.1	183	.2	0.57	82.3	129	.4	0.56
HD 183263 c	3.48	0.24	0.12	1329.2	7172	.2	0.16	461.6	760	.2	0.11	266.5	68	.1	0.15	230.8	40		157.97
HD 187123 b	0.51	0.01	117.95	2.4	18		353.88	0.8	17		349.54	0.5	16		363.63	0.4	14		357.38
HD 187123 c	1.94	0.25	0.10	1030.9	1619	.8	0.08	358.0	182	.8	0.11	206.7	50	.3	0.13	179.0	37	.1	0.14
HD 190360 b	1.54	0.31	0.13	2151.2	18797	.5	0.13	747.1	2013	.5	0.15	431.3	472	.5	0.15	373.6	276	.4	0.12
HD 190360 c	0.06	0.24	21.35	2.7	86		188.30	0.9	21		272.96	0.5	18		349.15	0.5	17		303.85
HD 192310 b	0.05	0.13	4.89	13.3	22		302.60	4.6	18		231.75	2.7	20		284.39	2.3	20		294.94
HD 192310 c	0.07	0.32	0.69	67.2	189	1.0	0.70	23.3	28	.3	0.69	13.5	15		250.01	11.7	15		284.48
HD 200964 b	1.95	0.04	0.60	155.3	601	.5	0.57	54.0	78	.3	0.59	31.1	31	.1	0.59	27.0	26		176.67
HD 200964 c	0.95	0.18	0.44	91.8	57	.1	0.40	31.9	17		290.15	18.4	14	.1	0.49	15.9	13		379.77
HD 202206 b	16.82	0.44	1.43	1542.5	38703	.9	1.43	535.7	4167	.9	1.43	309.3	1005	.9	1.43	267.8	603	.9	1.43
HD 202206 c	2.33	0.27	0.26	655.5	5898	.9	0.27	227.7	638	.7	0.27	131.4	151	.5	0.29	113.8	88	.3	0.29
HD 204313 b	3.50	0.23	0.19	1194.3	49648	.9	0.20	414.8	5468	.8	0.21	239.5	1439	.8	0.21	207.4	912	.9	0.21
HD 204313 d	1.61	0.28	0.13	719.4	275	.1	0.15	249.9	38	.2	0.15	144.3	20	.2	0.14	124.9	19	.1	0.11
HD 207832 b	0.56	0.13	2.26	34.5	42	.2	2.25	12.0	20		248.43	6.9	17		198.74	6.0	16		132.86
HD 207832 c	0.73	0.27	0.32	165.7	1305	1.0	0.32	57.6	141	1.0	0.31	33.2	36	.5	0.32	28.8	26	.1	0.31
HD 20794 b	0.01	0.00	19.94	1.3	20		321.46	0.5	20		296.47	0.3	20		296.47	0.2	20		296.47
HD 20794 c	0.01	0.00	9.11	2.0	13		308.78	0.7	13		326.50	0.4	13		333.67	0.3	13		350.99
HD 20794 d	0.01	0.00	4.04	6.7	10		279.35	2.3	10		293.67	1.3	9		288.36	1.2	9		244.85
HD 215497 b	0.02	0.16	92.84	0.1	18		287.48	0.0	22		330.92	0.0	19		293.38	0.0	19		265.21

				$i = 10^\circ$				$i = 30^\circ$				$i = 60^\circ$				$i = 90^\circ$			
Planet	$M_p \sin i$	e	$f_{\rm true}$	α	$\langle \Delta\chi^2 \rangle$	R	$\langle f_{\rm fit} \rangle$	α	$\langle \Delta\chi^2 \rangle$	R	$\langle f_{\rm fit} \rangle$	α	$\langle \Delta\chi^2 \rangle$	R	$\langle f_{\rm fit} \rangle$	α	$\langle \Delta\chi^2 \rangle$	R	$\langle f_{\rm fit} \rangle$
HD 215497 c	0.33	0.49	0.64	60.8	66	.6	0.64	21.1	12		189.00	12.2	12		302.23	10.6	12		268.00
HD 217107 b	1.40	0.13	51.25	26.3	188		81.29	9.1	29		253.43	5.3	19		348.28	4.6	18		331.45
HD 217107 c	2.62	0.52	0.09	3486.6	25193	.1	0.05	1210.9	2633	.2	0.09	699.1	566	.3	0.10	605.4	295		1.62
HD 37124 b	0.67	0.05	2.37	69.1	64		46.64	24.0	39		114.78	13.9	19		277.37	12.0	54		152.27
HD 37124 c	0.65	0.13	0.41	212.9	312	.1	0.46	73.9	15		136.66	42.7	9		208.23	37.0	16		280.50
HD 37124 d	0.69	0.16	0.20	370.2	2737	.2	0.20	128.6	302	.3	0.21	74.2	81	.1	0.22	64.3	8		323.07
HD 37605 b	2.80	0.68	6.64	99.3	55		12.85	34.5	19		306.28	19.9	15		243.46	17.2	14		240.91
HD 37605 c	3.37	0.01	0.13	1606.4	11737	1.0	0.14	557.9	1243	1.0	0.14	322.1	292	.6	0.15	279.0	177	.6	0.15
HD 38529 b	0.80	0.24	25.52	10.7	2875		2.66	3.7	329		43.36	2.1	92		93.06	1.9	53		179.41
HD 38529 c	12.26	0.36	0.17	4611.3	229061	.4	0.20	1601.5	24058	.4	0.20	924.6	5276	.6	0.19	800.7	2831	.6	0.19
HD 40307 b	0.01	0.00	84.72	0.3	20		341.29	0.1	20		324.61	0.1	20		324.61	0.1	20		324.61
HD 40307 c	0.02	0.00	37.97	1.0	11		245.60	0.3	12		259.32	0.2	12		257.48	0.2	12		286.04
HD 40307 d	0.03	0.00	17.85	2.1	7		361.02	0.7	7		382.69	0.4	7		385.23	0.4	7		387.42
HD 45364 b	0.19	0.17	1.61	26.2	21	.1	1.57	9.1	35		186.90	5.2	21		201.09	4.5	19		193.89
HD 45364 c	0.66	0.10	1.07	121.2	231	1.0	1.06	42.1	11	.1	1.05	24.3	9		384.50	21.1	8		386.28
HD 47186 b	0.07	0.04	89.42	0.5	15		245.26	0.2	35		281.03	0.1	20		211.43	0.1	19		240.70
HD 47186 c	0.35	0.25	0.27	116.6	228	1.0	0.27	40.5	11	.5	0.28	23.4	9		352.80	20.3	9		304.04
HD 4732 b	2.38	0.13	1.01	154.7	147	.3	1.03	53.7	27		148.10	31.0	14		186.82	26.9	34		146.48
HD 4732 c	2.36	0.23	0.13	594.0	1417	.3	0.14	206.3	158	.2	0.18	119.1	46		227.06	103.1	12		354.51
HD 60532 b	1.03	0.28	1.81	118.6	164	.6	1.82	41.2	29		86.73	23.8	17	.1	1.83	20.6	15	.1	1.83
HD 60532 c	2.46	0.02	0.60	587.4	6113	1.0	0.60	204.0	659	1.0	0.60	117.8	164	1.0	0.61	102.0	107	.9	0.61
HD 69830 b	0.03	0.10	42.14	1.3	19		294.62	0.4	17		366.09	0.3	17		320.10	0.2	17		320.10
HD 69830 c	0.04	0.13	11.57	3.5	8		329.35	1.2	8		336.45	0.7	7		373.63	0.6	7		391.12
HD 69830 d	0.06	0.07	1.85	18.3	4		387.30	6.4	4		359.11	3.7	4		346.32	3.2	4		356.91
HD 73526 b	2.86	0.19	1.94	99.4	725	.3	1.93	34.5	82	.1	1.94	19.9	28		144.98	17.3	25		148.75
HD 73526 c	2.42	0.14	0.97	134.0	137	.8	0.99	46.6	24	.1	1.00	26.9	18	.1	1.00	23.3	16		205.56
HD 74156 b	1.77	0.63	7.07	35.6	394		21.82	12.4	46		141.52	7.1	19		248.67	6.2	17		309.28
HD 74156 c	8.25	0.38	0.14	2216.8	32751	.4	0.17	769.9	3437	.5	0.16	444.5	772	.2	0.17	384.9	462	.1	0.10
HD 82943 b	1.59	0.20	0.83	332.7	2123	.8	0.83	115.6	234	.6	0.84	66.7	18	.3	0.85	57.8	15	.1	0.82
HD 82943 c	1.59	0.43	1.67	208.4	432	.6	1.66	72.4	54	.1	1.68	41.8	66		178.80	36.2	46		136.53
HD 9446 b	0.70	0.20	12.15	13.9	16		189.28	4.8	31		179.81	2.8	20		230.35	2.4	19		271.37
HD 9446 c	1.82	0.06	1.89	124.6	189	1.0	1.89	43.3	12	.4	1.89	25.0	10		404.08	21.6	9		384.89
HIP 14810 b	3.87	0.14	54.73	27.9	50		212.09	9.7	15		274.62	5.6	23		232.19	4.8	19		300.95
HIP 14810 c	1.28	0.15	2.47	72.3	22		153.44	25.1	43		184.65	14.5	9		428.63	12.5	9		268.37
HIP 14810 d	0.58	0.17	0.38	113.8	328	.9	0.39	39.5	8	.2	0.38	22.8	6		369.29	19.8	5		359.25
HIP 57274 b	0.04	0.19	44.90	0.8	26		252.25	0.3	18		317.57	0.2	27		287.94	0.1	25		276.96
HIP 57274 c	0.41	0.05	11.40	21.2	13		241.79	7.4	9		322.01	4.2	14		271.85	3.7	12		322.14
HIP 57274 d	0.53	0.27	0.85	154.6	503	1.0	0.85	53.7	59	.6	0.84	31.0	8		328.51	26.9	7		353.03
mu Ara b	1.75	0.13	0.57	823.9	50117	1.0	0.56	286.1	5132	1.0	0.57	165.2	1077	1.0	0.56	143.1	568	1.0	0.56
mu Ara c	1.89	0.10	0.09	3117.9	18667	.2	0.08	1082.8	1987	.2	0.09	625.2	416	.4	0.10	541.4	197	.1	0.12
mu Ara d	0.03	0.17	37.89	1.0	1203		1.02	0.3	120		9.80	0.2	58		175.61	0.2	33		216.38
mu Ara e	0.54	0.07	1.18	157.8	2475	.1	1.17	54.8	264	.1	1.17	31.6	28	.1	1.18	27.4	19	.1	1.17
upsilon And b	0.67	0.01	79.11	12.4	1723		20.99	4.3	180		29.89	2.5	49		184.59	2.1	101		146.02
upsilon And c	1.92	0.22	1.51	495.7	6356	.7	1.50	172.1	686	.7	1.50	99.4	179	.6	1.50	86.1	34	.3	1.50
upsilon And d	4.12	0.27	0.29	3232.5	215528	1.0	0.29	1122.6	23092	1.0	0.28	648.2	5530	1.0	0.28	561.3	3327	1.0	0.28